POLITECNICO DI TORINO

Collegio di Ingegneria Chimica e dei Materiali

Master of Science Course

in Materials Engineering for Industry 4.0

Master of Science Thesis

Optimization Of Thin Film Production from Nanomaterial Colloidal Inks By Ultrasonic Spray Coating and Their Usage in Hydrogen Evolution Reactions



Politecnico di Torino

Tutors:

Prof. Teresa Gatti

Dr. Mengjiao Wang

Candidate:

Beril Esra Ikizek

Settembre 2026

Abstract

In this study, catalysts for hydrogen evolution reactions (HER) were produced by spraying colloidal inks onto carbon paper using an ultrasonic spray coating method, and the effects of production parameters on catalytic performance were investigated. The three catalyst materials investigated were kesterite (CZTS), cobalt selenite (CoSe), and ruthenium-decorated cobalt selenite (RuCoSe). Three main parameters were varied during spraying: drying temperature, nozzle-substrate spray distance, and the number of layers applied. For CZTS, the parameters were optimized; it was found that the most critical parameter determining film morphology was the drying temperature, and that the parameter set allowing controlled evaporation provided the highest catalytic activity. The optimum CZTS sample was also photoelectrochemically characterized, revealing that the material is light responsive. Parameter analysis performed on CoSe and RuCoSe revealed that the presence of ruthenium improved both catalytic performance and electrochemically active surface area. It was concluded that CoSe performance increased with increasing number of layers, while RuCoSe showed the highest performance at an optimum thickness. The catalysts were characterized by cyclic voltammetry, linear sweep voltammetry, electrochemical impedance spectroscopy, Tafel slope analysis, electrochemically active surface area measurement, and stability tests. The findings reveal that ultrasonic spray coating parameters have a decisive effect on catalyst film performance and require separate optimization for each catalyst.

Table of Contents

Abstract i
List of Figures iii
List of Tables v
1. INTRODUCTION 1
2. MATERIALS & METHODS 5
2.1. Synthesis of the Electrocatalysts 5
2.2. Colloidal Ink Preparation and Formulations 6
2.3. Substrate Selection & Preparation 6
2.4. Ultrasonic Spray Coating 7
2.5. Hydrogen Evolution Reaction Experiment 9
2.5.1. Cyclic Voltammetry (CV) 10
2.5.2. Linear Sweep Voltammetry (LSV) 10
2.5.3. Tafel Slope Plot 11
2.5.4. Electrochemical Impedance Spectroscopy (EIS) 11
2.5.5. Electrochemically Active Surface Area (ECSA) 11
2.5.6. Chronopotentiometry 12
2.5.7. Chronoamperometry 12
3. RESULTS & DISCUSSION 13
3.1. CZTS 13
3.1.1. Spray-Distance Effects at 150 °C 13
3.1.2. Spray-Distance Effects at 200 °C 18
3.1.3. Influence of Layer Number at 150 °C and Z20 24
3.1.4. Platform-Temperature Comparison and Integrated Optimization 26
3.1.5. Photoelectrochemical Response and Stability of the Optimum CZTS Film 29
3.2. Cobalt Selenide (CoSe) 31
3.2.1. Influence of Distance 31
3.2.2. Influence of Coating Layers 36
3.3. Ruthenium-Decorated Cobalt Selenide (RuCoSe) 40
3.3.1. Influence of Distance 40
3.3.2. Influence of Coating Layers 44
3.4. RuCoSe and CoSe Comparison 49
4. CONCLUSION & PERSPECTIVE 53
REFERENCES 55

List of Figures

Figure 1. LSV curves of 10-layer CZTS films deposited at 150 °C using different spray distances. 14
Figure 2. Tafel plots of 10-layer CZTS films deposited at 150 °C using different spray distances. 14
Figure 3. Nyquist plots of 10-layer CZTS films deposited at 150 °C using different spray distances and measured at (a) −0.3 V and (b) −1.0 V versus RHE. 15
Figure 4. LSV curves of 20-layer CZTS films deposited at 150 °C using different spray distances. 15
Figure 5. Tafel plots of 20-layer CZTS films deposited at 150 °C using different spray distances. 16
Figure 6. Nyquist plots of 20-layer CZTS films deposited at 150 °C using different spray distances and measured at (a) −0.3 V and (b) −1.0 V versus RHE. 16
Figure 7. LSV curves of 30-layer CZTS films deposited at 150 °C using different spray distances. 17
Figure 8. Tafel plots of 30-layer CZTS films deposited at 150 °C using different spray distances. 17
Figure 9. Nyquist plots of 30-layer CZTS films deposited at 150 °C using different spray distances and measured at (a) −0.3 V and (b) −1.0 V versus RHE. 18
Figure 10. LSV curves of 10-layer CZTS films deposited at 200 °C using different spray distances. 19
Figure 11. Tafel plots of 10-layer CZTS films deposited at 200 °C using different spray distances. 19
Figure 12. Nyquist plots of 10-layer CZTS films deposited at 200 °C using different spray distances and measured at (a) −0.3 V and (b) −1.0 V versus RHE. 20
Figure 13. LSV curves of 20-layer CZTS films deposited at 200 °C using different spray distances. 20
Figure 14. Tafel plots of 20-layer CZTS films deposited at 200 °C using different spray distances. 21
Figure 15. Nyquist plots of 20-layer CZTS films deposited at 200 °C using different spray distances and measured at (a) −0.3 V and (b) −1.0 V versus RHE. 21
Figure 16. LSV curves of 30-layer CZTS films deposited at 200 °C using different spray distances. 22
Figure 17. Tafel plots of 30-layer CZTS films deposited at 200 °C using different spray distances. 23
Figure 18. Nyquist plots of 30-layer CZTS films deposited at 200 °C using different spray distances and measured at (a) −0.3 V and (b) −1.0 V versus RHE. 23
Figure 19. LSV curves of CZTS films containing different numbers of layers and deposited at 150 °C and Z20. 24
Figure 20. Tafel plots of CZTS films containing different numbers of layers and deposited at 150 °C and Z20. 25
Figure 21. Nyquist plots of CZTS films containing different numbers of layers and deposited at 150 °C and Z20, measured at (a) −0.3 V and (b) −1.0 V versus RHE. 25

Figure 22. LSV curves of Z20–10L CZTS films prepared at platform temperatures of 100, 150, and 200 °C. 26
Figure 23. Tafel plots of Z20–10L CZTS films prepared at 100, 150, and 200 °C. 27
Figure 24. Nyquist plots of Z20–10L CZTS films prepared at different platform temperatures and measured at (a) −0.3 V and (b) −1.0 V versus RHE. 28
Figure 25. Dark and illuminated LSV curves of the optimized CZTS film in (a) neutral and (b) acidic electrolyte. 29
Figure 26. Chopped-light chronoamperometry of the optimized CZTS film in (a) 0.5 M Na_2SO_4 at −0.6 V and (b) 0.5 M H_2SO_4 at −0.2 V versus RHE. 30
Figure 27. Chronopotentiometric response of the optimized CZTS film in 0.5 M Na_2SO_4 (pH 7) under constant cathodic current for approximately 13,000 s. 31
Figure 28. CV of CoSe films coated (150 °C, 10 L) with different distances from a)10 mm, b)20 mm, c)30 mm and d)40 mm. 32
Figure 29. LSV Results for Distance Comparison (CoSe 150C 10L) 33
Figure 30. Tafel Slope Analysis for Distance Comparison (CoSe 150 °C 10 L) 34
Figure 31. EIS Results for Distance Comparison (CoSe 150 °C 10 L) at a) -0.2 V, b) -0.4 V, and c) -0.5 V 35
Figure 32. CV Results of a) Uncoated C-paper and CoSe Films (150 °C, Z20) coated with b) 10 layers, c) 20 layers, d) 40 layers, e) 80 layers, f) 120 layers, g) 160 layers, and h) 200 layers 36
Figure 33. LSV Results for Number of Layers Comparison (CoSe 150C Z20) 37
Figure 34. Tafel Slope Analysis for Number of Layers Comparison (CoSe 150C Z20) 38
Figure 35. EIS Results for Number of Layers Comparison (CoSe 150C Z20) at a) -0.2 V, b) -0.4 V and c) -0.5 V 39
Figure 36. CV of RuCoSe films coated (150 °C, 10 L) with different distances from a)10 mm, b)20 mm, c)30 mm and d)40 mm. 41
Figure 37. LSV Results for Distance Comparison (RuCoSe 150C 10L) 42
Figure 38. Tafel Slope Analysis for Distance Comparison (RuCoSe 150C 10L) 43
Figure 39. EIS Results for Distance Comparison (RuCoSe 150C 10L) at a) -0.2 V, b) -0.4 V, and c) -0.5 V 43
Figure 40. CV Results of RuCoSe Films (150 °C, Z20) coated with a) 10 layers, b) 20 layers, c) 40 layers, d) 80 layers, e) 120 layers, f) 160 layers, g) 200 layers and h) Uncoated C-paper 45
Figure 41. LSV Results for Number of Layers Comparison (RuCoSe 150C Z20) 46
Figure 42. Tafel Slope Analysis for Number of Layers Comparison (RuCoSe 150C Z20) 47
Figure 43. EIS Results for Number of Layers Comparison (RuCoSe 150C Z20) at a) -0.2 V, b) -0.4 V and c) -0.5 V) 48
Figure 44. XRD of CoSe & RuCoSe 50
Figure 45. CP Results of RuCoSe & CoSe 51

List of Tables

Table 1. Ultrasonic Spray Coater Parameters 8
Table 2. Catalyst Production Parameters 9
Table 3. HER Set-Up 10
Table 4. Distance giving the strongest response for each electrochemical descriptor. 28
Table 5. ECSA Results for Distance Comparison (CoSe 150C 10L) 35
Table 6. ECSA Results for Number of Layers Comparison (CoSe 150C Z20) 39
Table 7. ECSA Results for Distance Comparison (RuCoSe 150C 10L) 44
Table 8. ECSA Results for Number of Layers Comparison (RuCoSe 150C Z20) 49
Table 9. 150C Z20 80L RuCoSe & CoSe HER Results 50

1. INTRODUCTION

Fossil fuels have been used as the main energy source for hundreds of years, but they bring with them major problems such as limited storage capacity and being one of the main causes of environmental pollution. Therefore, the interest in and urgency of the search for sustainable and environmentally friendly alternative energy sources is increasing every day. Hydrogen (H_2) stands out because it has the highest gravimetric energy density among all known fuels and is compatible with electrochemical energy conversion processes that do not produce CO_2 emissions.(McCay and Shafiee, 2020)

For all these reasons, finding a sustainable and low-energy consumption method of H_2 production has become an important issue among scientists. Hydrogen production methods can be classified as electrochemical, thermochemical, photochemical, radiochemical, biochemical, and hybrid. Today, most of the H_2 used for industrial purposes is produced using methods such as steam reforming or partial oxidation of natural gas or methane. This reveals that 96% of H_2 production technologies are based on non-renewable resources.(Ahmaruzzaman *et al.*, 2025)

In contrast to these traditional techniques, environmentally friendly alternative methods such as water splitting, biohydrogen, and methane pyrolysis are gaining prominence.(Kumar, Kumar and Pal, 2021)

Among these environmentally friendly alternatives, electrochemical water splitting stands out compared to other methods, particularly due to its advantages such as its ability to operate with renewable energy sources (solar, wind), its production of high-purity hydrogen, and its scalability. Currently, its most significant disadvantage is its cost, limit the large-scale industrialization of electrocatalytic H_2 production. Therefore, efforts to reduce costs largely focus on catalyst development. To evaluate the catalyst's function in the reaction, it is first necessary to understand the underlying mechanism by which HER occurs. Water splitting consists of two half-reactions: the hydrogen evolution reaction (HER) which takes place at the cathode, and the oxygen evolution reaction (OER) which takes place at the anode. This study focuses on the HER half-reaction in which hydrogen is directly produced. HER exhibits different behaviors depending on the pH of the electrolyte; therefore, each material, parameter, and experimental condition used in H2 production significantly affects and even alters the process. In an acidic environment, the reaction occurs via the reduction of protons ($2H^+ + 2e^- \rightarrow H_2$); while in neutral and alkaline environments, it occurs via the reduction of water molecules ($2H_2O + 2e^- \rightarrow H^2 + 2OH^-$).(Kahyarian, Singer and Nesic, 2016) The reaction generally occurs in two basic steps: first, a proton (or water molecule) combines with an electron to form adsorbed hydrogen (H_{ads}) on the electrode surface (Volmer step); then, the adsorbed hydrogen is converted into H_2 gas either by the reduction of a second proton (Heyrovsky step) or by the fusion of two adsorbed hydrogens (Tafel step).(Qadeer *et al.*, 2024) Although higher proton concentrations in acidic environments generally provide HER kinetics compared to alkaline environments, the acidity/basicity of the environment is influential in determining the dominant reaction and the required overpotential.(Qadeer *et al.*, 2024)

Additionally, the efficiency of water splitting depends on the electrocatalyst type. Given this situation, searching for more efficient and economical catalysts becomes a fundamental problem to be solved. The most active catalysts for HER are platinum and platinum group metals; these metals lower the activation energy by providing suitable active sites for proton adsorption.(Qadeer

et al., 2024) However, platinum belongs to the platinum-group metals classified by the European Union as critical raw materials, and its exceptionally high cost, low natural abundance, geographically concentrated production, and strong competing demand from sectors such as automotive manufacturing substantially constrain its widespread deployment.(Qadeer *et al.*, 2024) Therefore, scientific interest has turned to abundant and low-cost transition metals (iron, nickel, cobalt, copper) and their compounds in order to reduce the cost of the catalysts while achieving as good catalytic properties as possible. (Wang *et al.*, 2018)

Cu_2ZnSnS_4 (CZTS) is a multi-component sulfide composed of comparatively abundant elements and is best known as a light-absorbing semiconductor for thin-film photovoltaics. Its application has gradually expanded to electrocatalysis because its multinary framework, accessible kesterite and wurtzite phases, and composition-dependent defect chemistry provide considerable opportunities for tuning its surface and electronic properties. Surfactant-free CZTS nanoparticles are among the first CZTS materials known to catalyze both hydrogen and oxygen evolution, revealing the potential of this semiconductor beyond conventional methods.(Kush *et al.*, 2015)

Further studies have shown that nano structuring can increase the electrochemically accessible surface area and shorten charge transport distances, thereby improving HER activity.(Digraskar *et al.*, 2017) However, pure CZTS generally exhibits only moderate HER kinetics because of its semiconducting character, limited electrical conductivity, insufficient exposure of catalytically active sites, and non-optimal adsorption energetics. Accordingly, metal doping, stoichiometric control, void engineering, and incorporation with conductive carbon materials have been investigated. For example, it has been found that the addition of Co and graphene oxide hybridization improves charge transfer and enhances the HER performance of CZTS-based catalysts.(Digraskar et al., 2018, 2019).

Recent results demonstrate that the HER activity of CZTS is dependent on both morphology and cation stoichiometry, and that its catalytic properties cannot be understood solely from the Cu_2ZnSnS_4 composition.(Hu *et al.*, 2024) Cobalt selenites constitute another versatile link in HER electrocatalysts. Multiple accessible compositions, including CoSe, $CoSe_2$, and Co_3Se_4, provide tunable Co coordination, conductivity, and adsorption properties. Both cobalt and selenium sites can participate in interfacial charge redistribution, while nano structuring and defect formation can expose coordinatively unsaturated sites. An amorphous CoSe film electrodeposited directly on Ti mesh required an overpotential of only 121 mV to deliver 10 mA cm^{-2} for the HER under strongly alkaline conditions, demonstrating that CoSe can function as an active, self-supported cathode.(Liu et al., 2015; Dixit et al., 2018). Similarly, in a study with $CoSe_2$ nanoparticles grown on carbon fiber paper, it was observed that 100 mA cm^{-2} was generated at an overpotential of approximately 180 mV in an acidic electrolyte and maintained its activity and stability during long-term operation.(Kong et al., 2014). On the other hand, HER activity was obtained compared to the performance of solution-treated phase-pure $CoSe_2$ films, highlighting the importance of phase purity and scalable electrode production.(Kong et al., 2014). Despite these results, unmodified cobalt selenides are generally less active than platinum group metal catalysts, especially at the relevant current densities, and their performance can be affected by phase transformation, selenium loss, surface oxidation, and electrochemical remodeling during operation.

Adding ruthenium to cobalt-selenium offers an effective strategy to overcome these limitations while maximizing the use of precious metals. While Ru possesses high HER activity, the CoSe substrate can disperse Ru species, provide complementary adsorption sites, and modify their

structures via interfacial charge transfer. Since Ru itself is a rare and critical platinum group metal, the aim of this approach is not simply to replace Pt with another precious metal, but to achieve high activity using the least possible Ru loading. Decorating with Ru can optimize hydrogen adsorption at Ru sites, facilitate water activation under alkaline conditions, and reduce interfacial charge transfer resistance. Importantly, Ru–CoSe should not be considered as a structurally static catalyst. Under acidic HER conditions, it has been observed that hexagonal CoSe nanocrystals decorated with Ru clusters transform into a composite containing cubic $CoSe_2$, cobalt oxide/hydroxide species, and clustered Ru nanocrystals. The Ru–CoOx/Co(OH)x–$CoSe_2$ interface showed increased HER activity, indicating that the catalytically active state can be significantly different from the initially synthesized material.(Wang et al., 2019).

More recently, the addition of Ru to Se-vacancy-rich $CoSe_2$ optimized hydrogen adsorption by creating electron-rich Ru sites via Co–Se–Ru charge transfer, reducing the alkaline HER overpotential to 29 mV at 10 mA cm^{-2}; the Ru bulk activity was 44.2 Å $mgRu^{-1}$ (Liu et al., 2024). In summary, CZTS, CoSe, and Ru–CoSe represent three complementary stages in chalcogenide-based HER catalyst design: a multi-component platinum group metal-free sulfide with highly tunable composition, a naturally more active cobalt selenide platform, and a Ru-modified heterointerface that maximizes the use of small amounts of precious metal. Systematic comparison of these materials can clarify how chalcogen identity, phase composition, defect structure, interfacial electronic coupling, and electrochemical remodeling govern HER kinetics. This kind of understanding is essential for designing robust and resource-efficient electrocatalysts that combine the structural versatility of multi-component chalcogenides with the high intrinsic activity of precisely distributed Ru sites.

In addition, the actual performance of a catalyst depends not only on the material itself but also on how homogeneously, stably, and reproducibly it is transferred to the electrode surface. This is where colloidal inks come to the forefront. Colloidal ink is a suspension in which catalyst nanoparticles are stably dispersed in a suitable solvent.(Zhang *et al.*, 2020) Since a large portion of nanomaterials are already synthesized in colloidal suspension form, converting these particles directly into a dispersible ink is a practical way to transfer them to the electrode surface.(Wang *et al.*, 2023) Because colloidal ink formulation can be controlled through parameters such as solvent type, particle concentration, and stability, it directly determines the macroscopic properties of the ink, such as viscosity, surface tension, aggregation, and rheology; these properties directly affect the homogeneity, thickness, adhesion and microstructure of the film formed after coating.(Pozzati *et al.*, 2024; Wang *et al.*, 2024) This is a critical step affecting the actual electrocatalytic performance of the catalyst. The focus of this study is shaped by the current problems and needs mentioned above. The production chain from colloidal ink to thin film, ink formulation, coating method, and coating parameters constitute critical stages determining the quality of this transfer. Therefore, this thesis aims to optimize the coating process in the conversion of different nanomaterial colloidal inks into thin films via ultrasonic spray coating, and the performance of the resulting films is evaluated through HER, a cathodic half-reaction in which hydrogen is directly produced. The optimization aims to systematically determine the spray parameters that yield the highest electrocatalytic activity for each material.

In this context, three different nanomaterial catalysts were investigated: CZTS (Cu_2ZnSnS_4, kesterite), CoSe, and RuCoSe. CZTS was chosen because it is a low-cost polymetallic sulfide composed of elements abundant on Earth. CoSe, because it is a transition metal diselenide exhibiting effective HER activity in an acidic environment, and RuCoSe, because it allows

investigation of the effect of ruthenium doping and rough morphology on catalytic performance. These catalyst powders were prepared as colloidal inks in isopropyl alcohol and deposited onto plasma-cleaned carbon paper, which was treated to remove surface contaminants before coating, using an ultrasonic spray coating. During the coating process, parameters such as spray distance, number of layers, and drying temperature were systematically varied. The effects of these parameters on film quality and HER performance were evaluated by measuring electrocatalytic performance tests.

The thesis is structured as follows: The first section addresses the scope, motivation, and purpose of the study and discusses the literature and theoretical background regarding the hydrogen evolution reaction, the catalyst materials studied, and the production methods used, highlighting comparisons and identifying gaps in the literature that also motivated this study. The second section describes in detail the materials used, ink preparation, the surface treatment method used for substrate preparation, ultrasonic spray coating, and electrochemical characterization methods. The parameters used throughout the process are clearly stated. The third section presents the CV, LSV, EIS, ECSA, and CP results obtained for the three materials and discusses them comparatively with the literature, describing the optimum parameters for different thin films. The fourth section concludes the main results obtained from the measurements and offers suggestions for future research.

2. MATERIALS & METHODS

This section describes in detail the materials used and the experimental methods applied in this study. First, the catalyst materials examined are described in general terms; then, the preparation of colloidal inks, the plasma-cleaning treatment of carbon paper substrates, and the deposition of thin films by ultrasonic spray coating are explained. The parameters examined in the spray coating process and the electrochemical experimental setup used in hydrogen evolution reaction (HER) measurements are described; finally, the electrochemical measurement techniques applied in the characterization of the films are presented along with the HER mechanism.

2.1. Synthesis of the Electrocatalysts

In this study, three different powder catalysts were used: CZTS, CoSe, and RuCoSe.

Synthesis of CZTS NCs: Copper(II) acetate monohydrate [$Cu(CH_3COO)_2 \cdot H_2O$, Carlo Erba], zinc(II) acetate [$Zn(CH_3COO)_2$, Thermo Scientific], tin(IV) chloride pentahydrate ($SnCl_4 \cdot 5H_2O$, ≥ 98%, Acros Organics), elemental sulfur (S, 99.98%, Sigma-Aldrich), and oleylamine (OLA, technical grade, 70%, Sigma-Aldrich) were used as received. CZTS nanocrystals (NCs) were synthesized following a literature procedure based on the thermal decomposition of inorganic precursors in a high-boiling nonpolar solvent, similar to the method reported by Y. Qu et al. (Qu *et al.*, 2014) Briefly, 0.9 mmol of $Cu(CH_3COO)_2 \cdot H_2O$, 0.5 mmol of $Zn(CH_3COO)_2$, and 0.5 mmol of $SnCl_4 \cdot 5H_2O$ were dissolved in 25 mL of OLA preheated to 50 °C in a three-necked flask connected to a Schlenk line. The mixture was heated to 100 °C and purified with N_2 for 1 h. Then the temperature was increased to 225 °C, followed by the rapid injection of 5 mL of a 3.6 M sulfur–OLA solution. The reaction mixture was held at 225 °C for 1 h under N_2 to promote NC growth. After cooling, the NCs were purified through three centrifugation cycles at 7800 rpm using a 1:6 (v/v) toluene/acetone mixture and followed by air drying. The resulting powder was annealed in an N_2–purified tube furnace under continuous flow of N_2 at atmospheric pressure. The temperature was increased to 450 °C at 6 °C min^{-1}, maintained for 1 h, and then allowed to cool naturally under N_2.

Synthesis of CoSe and Ru–CoSe NCs.: Cobalt(II) acetylacetonate [$Co(acac)_2$, 99.99%], ruthenium(III) chloride hydrate ($RuCl_3 \cdot xH_2O$), 1-octadecene (ODE, 90%), oleylamine (OAm, 70%), ethanol (99.9%), toluene (99.7%), and sulfuric acid (H_2SO_4) were purchased from Sigma-Aldrich, while selenium powder (99.99%) was obtained from Strem Chemicals; all reagents were used as received, and $Co(acac)_2$ and Se were stored in an N_2-filled glovebox. CoSe and RuCoSe NCs were synthesized according to the same procedure.(Wang *et al.*, 2019) To prepare the Se–OAm precursor, 8 mmol of Se powder was mixed with 24 mL of OAm and degassed under vacuum at 120 °C for 1 h. The mixture was rapidly heated to 180 °C and then gradually to 230 °C, and held at this temperature for approximately 3 hours until a clear orange solution was obtained. The precursor was stored in an N_2-filled glovebox. For the synthesis of Ru–CoSe NCs, 0.05 mmol of $RuCl_3 \cdot xH_2O$ and 1 mmol of $Co(acac)_2$ were mixed with 10 mL of ODE in a 25 mL round-bottom flask and degassed under vacuum at 120 °C for 1 h. A portion of the Se–OAm precursor containing 1 mmol of Se was then injected under N_2. The mixture was heated to 250 °C and maintained at this temperature for 5 min while stirring. The resulting black product was purified twice by redispersion in toluene and precipitation with ethanol. Finally, the nanocrystals were annealed at 400 °C for 30 minutes under a continuous flow of N_2 to thermally decompose the residual ligands on the surface.

Pure CoSe nanocrystals were prepared using the same procedure without the addition of the Ru precursor.

The three materials selected in this study will also offer the opportunity to evaluate ultrasonic spray coating optimization in different material classes and under different electrolyte conditions. Thus, the effects of spray parameters can be compared across different chemical structures and conditions, without being limited to a single material.

2.2. Colloidal Ink Preparation and Formulations

Colloidal inks were prepared by dispersing catalyst powder in isopropanol (IPA). For each ink, 10 mg of catalyst powder was added to 20 mL of IPA to obtain a suspension at a concentration of 0.5 mg/mL. The properties of the powders used as catalysts and the advantages they can offer in this study are described in section 2.1. Isopropanol (IPA) was used as the solvent. IPA has many advantages such as high zeta potential, a suitable dielectric constant, and low surface tension.(Shukla et al., 2017). Its low surface tension ensures good spreading and improves wetting, resulting in a more homogeneous film. It is the solvent with the strongest colloidal stability and is suitable for ultrasonic spray coating.(Shukla *et al.*, 2017) The formulation consists only of powder and IPA. Before use in ultrasonic spray coating, the prepared ink was homogenized by mixing in an ultrasonic bath sonicator for 1 hour. Approximately 0.2 mL of ink was sprayed onto the substrate in each layer. Accordingly, the total ink volume and catalyst loading applied increase proportionally with the number of layers.

2.3. Substrate Selection & Preparation

Carbon paper has been chosen as a substrate for coating catalyst films due to its porous structure, high electrical conductivity, and chemical stability under varying pH conditions. (Li et al., 2024). Its porous and conductive structure allows for uniform electron transfer to the catalyst layer and acts as a gas diffusion layer, allowing hydrogen bubbles formed during HER to easily escape from the electrode surface. Furthermore, its mechanical strength and flexibility help maintain its structural integrity throughout spraying and electrochemical measurements. It stands out in the industry because it is lighter and more durable than most materials and can be easily scaled. These properties make carbon paper a reliable electrode surface that closely resembles real-world application conditions.

Surface treatment, which prepares the surface for thin film deposition before coating, is one of the factors that improves surface quality. By adding oxygen-containing functional groups (such as hydroxyl or carboxyl groups) to the naturally hydrophobic graphite surface, the carbon paper is made even more hydrophilic.(Ortiz-Ortega et al., 2021). The aim is to obtain a more homogeneous film by improving surface activation. Therefore, surface treatment was determined as the first step in substrate preparation. Plasma cleaning was chosen and applied to all C-papers used in the study. Surface cleaning and modification were performed using reactive plasma created in a low-pressure gas environment. O_2 plasma was used in the process, thus cleaning the surface, removing impurities, and eliminating physically adsorbed components.(Ortiz-Ortega et al., 2021). This increased surface energy and improved wettability, allowing the IPA-based ink to wet the substrate better. (Armbruster et al., 2025). The most critical detail at this stage is that plasma cleaning is a temporary activation, and the surface returns to its original state over time. This is called hydrophobic recovery. Therefore, spray coating was completed without delay after surface treatment.(Ortiz-Ortega et al., 2021).

After treatment, the C-paper, with improved properties and ready for ink application, was cut into 2 cm x 1 cm sections for each measurement. Applications were then performed to cover a 1 cm^2 area of these prepared C-papers; current density calculations were also based on this covered area.

2.4. Ultrasonic Spray Coating

A coating method called ultrasonic spray coating breaks a liquid solution into a tiny mist of equally sized droplets using high-frequency vibrations. Ultrasonic spray coating is based on the principle of converting a liquid ink into an aerosol through ultrasonic vibrations, and the resulting droplets coalescing on the substrate surface to form a film. Consequently, it makes it possible to deposit very thin, uniform, and regulated materials on a variety of surfaces.(Bose *et al.*, 2013)

The ultrasonic spray coating method was used in the conversion of colloidal inks into thin films. This method was preferred because it allows for the economical use of the limited amount of catalyst powder produced thanks to its high transfer efficiency, the independent control of droplet size and kinetic energy of the droplets, and the performance of repeatable thickness control over the number of layers. (Benramache, Benhaoua and Bentrah, 2013) In addition, being a contactless method, it makes it possible to obtain a smooth and consistent coating on porous, brittle, and rough substrates such as carbon paper.

In the experimental setup, the ink is fed into the ultrasonic nozzle at a constant flow rate via a syringe pump. The liquid reaching the nozzle tip is subjected to high-frequency mechanical vibrations generated by piezoelectric elements. These vibrations create capillary waves in the thin layer of liquid on the nozzle atomization surface. When a sufficient level is reached, cavitation occurs at the liquid-gas interface, and the liquid breaks off from the peaks of the capillary waves. (Bose et al., 2013). This mechanism produces an aerosol consisting of droplets with a narrow size distribution, directly related to the capillary wavelength. Therefore, the fundamental parameter determining droplet size in ultrasonic atomization is the applied vibration frequency; as the frequency increases, the capillary wavelength and consequently the droplet size decrease.

In ultrasonic systems, atomization occurs independently of the carrier gas; the carrier gas only serves to direct the resulting aerosol towards the substrate. Thus, droplet size (via frequency), kinetic energy of the droplets (via carrier gas pressure), and volume of liquid spray per unit time (via flow rate) can be adjusted independently. Furthermore, the gas used in this study is nitrogen. This independent control is a decisive advantage for this study, which aims at systematically optimizing spray parameters. Droplets released from the nozzle are transported to the substrate surface by the carrier gas flow. The time it takes for the droplets to reach the substrate and the solvent evaporation that occurs during this time directly determines the morphology of the film. According to these, two boundary regimes can be defined in the literature. In the "wet regime," the droplets arrive at the substrate largely in liquid form; a continuous liquid film forms on the substrate and then dries. In this case, edge accumulation ("coffee ring" effect) and thickness irregularities can be observed due to the movement of the solvent towards the edges. (Sliz, Czajkowski and Fabritius, 2020) In the "dry regime," the droplets dry largely before reaching the substrate; a porous and poorly adhering layer forms on the surface that cannot coalesce.(Bose *et al.*, 2013) Optimum film quality is obtained from a combination of properties between these two regimes. Increasing the nozzle-substrate distance and substrate temperature shifts the deposition from the wet regime to the dry regime. The droplets deposited on the substrate coalesce to form a continuous layer; this process is repeated to obtain a film of the desired thickness. In ultrasonic spray deposition, the

number of layers applied is related to the film thickness, providing a simple and repeatable control mechanism for catalyst loading.

Coating operations were performed using the Nadetech Innovations ND-SP model ultrasonic spray coating system. The system consists of an ultrasonic nozzle and generator unit, a syringe pump for ink supply, a carrier gas line, a programmable three-axis (x-y-z) motion system, and a temperature-controlled heater (hotplate). The colloidal ink, prepared before coating, was placed in the system using a 20 mm diameter syringe. Plasma-cleaned carbon paper substrates were placed on the pre-heated platform, and the platform temperature was allowed to stabilize. Before coating began, a 5-second stabilization period was applied to ensure a stable spray cone.

A rectangular area of 10 mm × 10 mm (total coating area of 1 cm^2) was selected as the coating pattern, and the nozzle was moved vertically across this area using a scanning motion. During scanning, the distance between successive lines was set to 2 mm. After each layer application, a 30-second waiting period was applied before proceeding to the next layer; this allowed the solvent to completely evaporate and the layer to dry. This waiting period is to prevent wet film deposition and associated thickness irregularities. After the coating process was completed, samples were taken for electrochemical measurements after cooling to room temperature. There are numerous parameters that affect film quality in ultrasonic spray coating. In this study, most system parameters were kept constant throughout the experiments; however, nozzle-substrate distance (Z), number of layers (L), and platform temperature (T) were systematically varied to investigate their effects on film properties and HER performance. Thus, the influence of other variables was eliminated, and the contribution of the three parameters under investigation was isolated.

***Table 1**. Ultrasonic Spray Coater Parameters*

Parameters	Value
Frequency	85-95 kHz
Nozzle Power	2.5 W
Max Load Power	5 W
Voltage	23.3 V
Carrier Gas Pressure	0.1 bar
Working Flow	25 mL/h
Speed	400 mm/min
Syringe Diameter	20 mm
Distance Between Steps	2 mm
Overage Distance Step	4 mm
Stabilize Spray Distance	2 mm
Waiting Time Between Layers	30 sec
Waiting Time Between Process	30 sec
Number of Cycles	1

Expected effects of the modified parameters:

Nozzle–substrate distance (Z): Determines the time it takes for droplets to reach the substrate and the solvent evaporation that occurs during this time. Increasing the distance causes the droplets to reach the surface in a drier state (because they are exposed to heat for a longer time before reaching the surface), shifting deposition to a dry regime; this can result in porous and poorly adhering films. Decreasing the distance leads to more liquid being released per unit area and an increase in film

thickness, but in extreme cases, there is a risk of wet film formation. In this study, the optimum operating range was determined by varying the Z parameter in the range of 10–40 mm.

Note: In this study, the abbreviations "Z10", "Z20", "Z30" and "Z40" represent nozzle–substrate distances of 10, 20, 30 and 40 mm, respectively.

Number of layers (L): The number of layers is a fundamental parameter determining the film thickness and, consequently, the catalyst loading per unit area. Increasing the number of layers increases the amount of active material and the number of potential active sites; however, excessive thickness can lengthen the electron transport path and limit mass transport. In this study, the number of layers varied between 10 and 200 depending on the material.

Platform temperature (T): This affects the evaporation rate of the solvent after each layer is deposited, thus affecting the drying behavior of the layer and the film morphology. Increasing the temperature accelerates evaporation, shifting the deposition to a dry regime. In this study, common platform temperatures of 150 °C and 200 °C were selected for comparison for all three catalysts. Additionally, comparisons for CZTS at 100 °C, 150 °C, and 200 °C are given below.

***Table 2**. Catalyst Production Parameters*

Material	Platform Temperature (T)	Nozzle–substrate Distance (Z)	Number of Layers (L)
CZTS	100°C-150°C-200°C	10-20-30-40	10-20-30
CoSe	150°C	10-20-30-40	10-20-40-80-120-160-200
RuCoSe	150°C	10-20-30-40	10-20-40-80-120-160

Sample Nomenclature:

The prepared samples are identified using a naming convention that follows the sequence of material, platform temperature, nozzle-substrate distance, and number of layers. For example, the expression "CZTS 150C Z20 20L" indicates a CZTS sample prepared at a platform temperature of 150 °C, a nozzle-substrate distance of 20 mm, and with 20 layers applied.

2.5. Hydrogen Evolution Reaction Experiment

The hydrogen evolution reaction (HER) is a fundamental half-reaction in which water or neutral/acidic/basic solutions are electrochemically reduced to hydrogen gas (H_2). Hydrogen evolution reaction (HER) measurements were performed using a three-electrode electrochemical cell setup and a potentiostat controlled by NOVA software. The setup consists of a working electrode, a reference electrode, and a counter electrode. As the working electrode, carbon paper coated with a catalyst film using ultrasonic spray coating was used; in measurements, a 1 cm^2 active area was brought into contact with the electrolyte, and current density calculations were performed based on this area. An Ag/AgCl electrode was used as the reference electrode. The counter electrode and electrolyte varied depending on the material being studied: Kesterite measurements were performed in a neutral electrolyte (0.5 M Na_2SO_4, pH 7) with a platinum counter electrode; CoSe and RuCoSe measurements were performed in an acidic electrolyte (0.5 M H_2SO_4, pH 0) with a graphite counter electrode. Due to this difference in electrolyte and counter electrode, a direct material comparison between CZTS and CoSe/RuCoSe was not performed; each material was evaluated according to its own electrolyte conditions.

Table 3. HER Set-Up

Material	Electrolyte	pH	Reference Electrode	Counter Electrode
CZTS	0.5M Na_2SO_4 & 0.5M H_2SO_4	7 & 0	Ag/AgCl	Platin (Pt)
CoSe	0.5M H_2SO_4	0	Ag/AgCl	Graphite
RuCoSe	0.5M H_2SO_4	0	Ag/AgCl	Graphite

All electrochemical measurements were performed at room temperature. No deaeration was applied to the electrolyte during the measurements; nitrogen was used only as a carrier gas during the spray coating stage.

All potentials obtained in the measurements were converted with respect to the reversible hydrogen electrode (RHE) for comparability. The following equation (2.1) was used in the conversion:

$$E(RHE) = E\left(\frac{Ag}{AgCl}\right) + 0{,}059 \times pH + E°\left(\frac{Ag}{AgCl}\right) \quad (2.1)$$

The HER performance of spray-formed catalyst films was evaluated using cyclic voltammetry (CV), linear sweep voltammetry (LSV), Tafel slope analysis, electrochemical impedance spectroscopy (EIS), electrochemically active surface area (ECSA), chronopotentiometry (CP), and chronoamperometry (CA) techniques, with the specified parameters. ECSA measurements were performed only for CoSe and RuCoSe samples. All measurements were carried out at room temperature using the three-electrode setup described in the previous section.

2.5.1. Cyclic Voltammetry (CV)

Cyclic voltammetry (CV) is a powerful and popular electrochemical technique commonly employed to investigate the reduction and oxidation processes of molecular species. CV is also invaluable to study electron transfer-initiated chemical reactions, which include catalysis. (Elgrishi *et al.*, 2018) In this study, CV measurements were performed to investigate the general electrochemical behavior of the catalyst and to determine its steady-state performance. The scan rate was set to 50 mV/s for all measurements, and 10 sequential scans were taken for each sample. The potential range varied depending on the electrolyte condition: −0.2 V to −1.2 V for CZTS (relative to Ag/AgCl); −0.2 V to −0.82 V for CoSe and RuCoSe (relative to Ag/AgCl). The second scan was considered the steady-state result to disregard the activation effects observed in the first scan. Inter-sample comparisons were made based on current densities at a potential of −0.6 V (RHE).

2.5.2. Linear Sweep Voltammetry (LSV)

Linear scan voltammetry (LSV), a simple potentiostatic scanning technique, measures current as a function of time while linearly scanning the working electrode potential between final and initial values. (Anita et al., 2023). LSV has been used as the first screening measurement in evaluating HER performance and determining optimum spraying parameters. The scan rate was set to 10 mV/s in all measurements. The potential range varied depending on the electrolyte condition: −0.2 V to −1.2 V for CZTS (relative to Ag/AgCl); −0.2 V to −0.8 V for CoSe and RuCoSe (relative to

Ag/AgCl). Current densities obtained from LSV curves were used as the basis for comparing samples with different spray parameters (distance, number of layers, temperature).

2.5.3. Tafel Slope Plot

A Tafel slope plot can be used to distinguish between kinetic and non-kinetic contributions to the Tafel slope value; kinetic meaningfulness is shown by a constant Tafel slope region.(van der Heijden et al., 2024). To evaluate HER kinetics, the Tafel slope was calculated by deriving it from LSV data. The slope of the linear region obtained from the graph plotted with the overpotential (η) and the logarithm of the current density (log j) was calculated as the Tafel slope (b) according to equation (2.2):

$$\eta = b * \log\left(\frac{j}{j_o}\right) \quad (2.2)$$

A lower Tafel slope indicates that the current density increases faster with overpotential, which indicates faster electron transfer kinetics.

2.5.4. Electrochemical Impedance Spectroscopy (EIS)

The basic principle of EIS is to apply a sinusoidal signal over a wide frequency range to perturb an electrochemical system in equilibrium or steady state. Then, the system's sinusoidal response (current or voltage, respectively) to the applied stimulus is observed. Since the electrochemical system under investigation is a linear and time-invariant system (i.e., the output signal is linearly related to the input signal and the system's behavior does not change over time), EIS is a "transfer function" technique that models the output signal as a function of the input signal over a wide frequency range. (Lazanas and Prodromidis, 2023).

EIS measurements were performed in potentiostatic mode to investigate the charge transfer kinetics at the electrode interface. All measurements were taken with a sinusoidal signal of 10 mV amplitude in the frequency range of 100 kHz to 0.1 Hz (10 points per decade). Measurement potential varies according to electrolyte conditions: −0.3 V, −0.6 V, and −1 V for CZTS; −0.2 V, −0.4 V, and −0.5 V for CoSe and RuCoSe. Charge transfer resistance (Rct) was interpreted from the obtained Nyquist plots by evaluating it according to the x-axis intersection at the low-frequency end of the semicircle. No estimation was made for incomplete semicircles; the relevant measurements were classified as "above the measurement limit".

2.5.5. Electrochemically Active Surface Area (ECSA)

The electrochemically accessible surface area of a catalyst that actively participates in redox processes is known as the electrochemical surface area, or ECSA. (Johnson Andi, 2025). ECSA, or the actual active surface area of an electrocatalyst, is a crucial parameter for determining the specific and overall activity of catalytic materials. Electrocatalyst performance can be compared using ECSA without considering structural elements such as porosity, charge, and distribution on conductive surfaces. Therefore, a more reliable method for selecting the most effective catalysts is to compare materials based on specific current density (current normalized to active surface area) rather than total current. (Johnson Andi, 2025).

Cyclic voltammetric methods offer several advantages in ECSA determination. These include the ability to assess catalyst surface stability and activation/deactivation events, compatibility with a wide range of electrocatalyst materials, and the provision of complementary data on electronic structure and reaction mechanisms.

Measurements were taken at 50, 100, 150, 200, and 250 mV, with each measurement containing 30 cycles. The last cycle was chosen during the calculation because the first cycles stabilize the surface. Data were collected at a potential of 0.14V. This region is where the current is almost flat/parallel to the potential and is ideal for reading capacitive current. When comparing calculations, a higher ECSA generally corresponds to a higher number of active regions, leading to improved reaction rates.

$$\Delta j = j_a - j_c \tag{2.3.}$$

$$C_{dl} = slope\left(\frac{\frac{\Delta j}{2}}{\nu}\right) \tag{2.4}$$

$$ECSA = \frac{C_{dl}}{C_s} \tag{2.5}$$

$$C_s = 40\ \frac{\mu F}{cm^2}$$

The electrochemically active surface area (ECSA) is determined from the double-layer capacitance (C_{dl}) using cyclic scans recorded over a non-faradayic potential range, in which no charge transfer reaction occurs and the measured current originates solely from the charging and discharging of the electrical double-layer.

CVs are summed at various scan rates (ν), and the capacitive current density at a constant potential in the middle of this range is considered as the difference between the anode and cathode and calculated using equation 2.3.

Half of the current difference (Δj) measured at each scan rate was plotted against the scan rate, and C_{dl} was calculated from the slope of the resulting line (equation 2.4). The electrochemically active surface area was found by dividing the C_{dl} value by the specific capacitance (C_s) value, as in equation 2.5; for an acidic environment, $C_s = 40\ \mu F/cm^2$ was taken as a reference. (Ramírez *et al.*, 2025)

2.5.6. Chronopotentiometry

When a current is delivered to the electrode in chronopotentiometry, the potential shifts to a point where the electroactive species' flux is adequate to supply the applied current.(Taherpour and Mousavi, 2018) CP was applied to evaluate the stability of catalyst films. The time-dependent variation of the electrode potential was monitored by applying a constant current density of 10 mA/cm². The attainment of a stable plateau in the potential overtime was considered an indicator of catalyst stability.

2.5.7. Chronoamperometry

Chronoamperometry measurements were also analyzed to investigate the electrochemical activity and stability of electrocatalysts.(Marcelo M. Tusi a, 2010) Unlike chronopotentimetry (CP), in this technique, the time-dependent change in current density was monitored over a period of time by applying a constant potential. The conservation of current density over time would be considered an indicator of catalyst stability.

3. RESULTS & DISCUSSION

In this section, the HER performance of CZTS, CoSe, and RuCoSe thin films as a function of spray coating parameters (distance, number of layers, and temperature) is evaluated using the results of LSV, EIS, ECSA, CP, CA, and Tafel slope analysis. The results are first presented separately for each material; then, CoSe and RuCoSe, tested under the same electrolyte conditions, are discussed comparatively. Since CZTS and CoSe/RuCoSe were tested with different electrolytes (neutral and acidic, respectively), a direct performance comparison between these two groups was not made; each material was evaluated within its own conditions. Additionally, for CZTS, a comparison was made using both acidic and neutral electrolytes. In addition, the difference between light and dark environments was determined by CZTS. LSV current density was used as the primary indicator in determining the optimum spray parameter.

3.1. CZTS

The electrochemical performance of CZTS films was optimized by investigating three interrelated ultrasonic sputtering parameters: nozzle-substrate distance, number of deposited layers, and platform temperature. Linear scanning voltammetry (LSV) was used as the primary parameter descriptor, while Tafel analysis and electrochemical impedance spectroscopy (EIS) provided complementary information on the potential dependence of current and impedance response. Rather than repeating the order in which individual measurements were obtained, the discussion was organized around sputtering distance, as it was most comprehensively investigated across this variable temperature-layer matrix. Therefore, the distance effects at 150 and 200 °C will be discussed first, followed by direct comparisons of number of layers and temperature, and an integrated selection of optimum coating conditions. The current densities mentioned below were read at -0.6 V relative to the reversible hydrogen electrode (RHE). Due to the unusually large Tafel slopes and the incompleteness of several Nyquist semicircles, both Tafel slopes and charge transfer resistances were treated as comparative descriptors.

3.1.1. Spray-Distance Effects at 150 °C

Since a large portion of the experimental matrix was systematically varied with various parameter sets, spray distance was chosen as the primary moderating variable. This variable controls the spraying time of the droplet, solvent loss before reaching the substrate, lateral dispersion, speed of surface arrival, and the area where the ink is deposited. Z10, Z20, Z30, and Z40 settings were first compared at 150 °C for 10, 20, and 30 layers.

3.1.1.1. Ten-Layer Films

Spray distance affects the lateral distribution, velocity, drying state, and impact behavior of droplets reaching the surface. Four settings, Z10, Z20, Z30, and Z40, were compared using 10 layers at 150 °C. Figure 1 shows the corresponding LSV curves. At −0.6 V, Z20 generated approximately −14 mA cm^{-2} of current, while Z10, Z30, and Z40 each generated approximately −11 mA cm^{-2}. Therefore, Z20 represented the strongest distance in the 10-layer LSV comparison and produced the highest current density in the full CZTS dataset. A possible geometric explanation for this could be that Z20 provides a balance between the excessive local deposition in Z10 and the material distribution beyond the 1 cm^2 target area in Z30-Z40. The related differences in thickness,

homogeneity and opacity were inferred from the deposition geometry rather than being determined directly quantitatively.

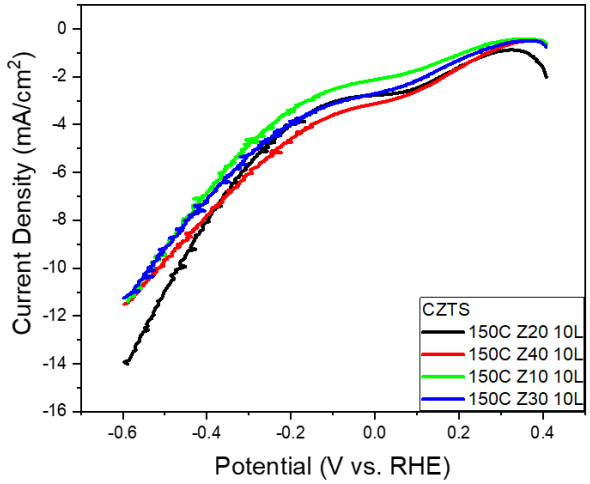


Figure 1. *LSV curves of 10-layer CZTS films deposited at 150 °C using different spray distances.*

The distance-dependent apparent Tafel slopes are shown in Figure 2. The fitted slopes increased with distance: 713 mV dec^{-1} for Z10, 754 mV dec^{-1} for Z20, 869 mV dec^{-1} for Z30, and 955 mV dec^{-1} for Z40. Although Z10 gave the lowest slope, it did not give the largest LSV current. This shows that the slope cannot be interpreted independently of the Tafel intercept, curve position, accessible area, and film resistance; the results of all characterization methods must be evaluated together.

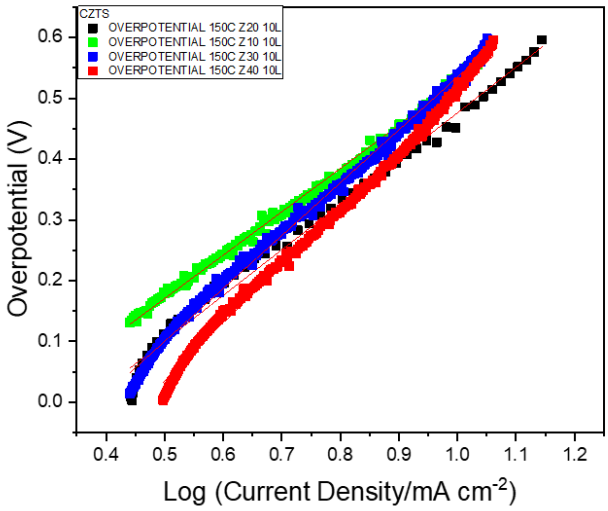


Figure 2. *Tafel plots of 10-layer CZTS films deposited at 150 °C using different spray distances.*

Nyquist plots for the same distance series are presented in Figure 3. At −0.3 V, the apparent Rct values are approximately 150 Ω for Z40, 200 Ω for Z20, 225 Ω for Z30, and 270 Ω for Z10. At −1.0 V, all distances are in the range of approximately 30–40 Ω and show two successive arc-like

curves. These characteristics indicate multiple time constants, but they cannot be uniquely assigned without fitting an equivalent circuit. The convergence at −1.0 V shows that the effect of the deposition geometry on the impedance response becomes less pronounced at larger driving forces. Z20 is retained as the selected spraying distance because LSV is the primary activity criterion and provides the highest absolute cathodic current.

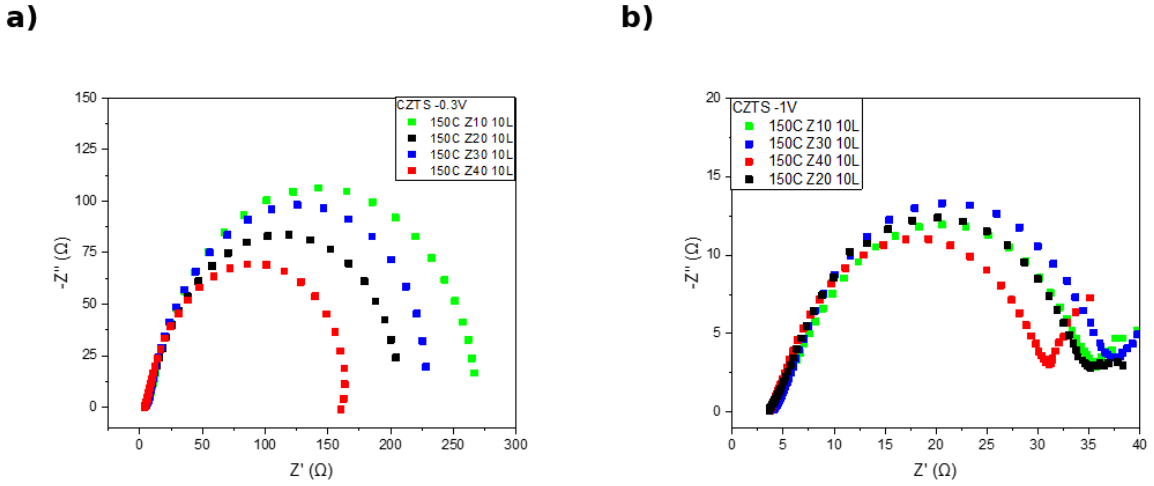


Figure 3. *Nyquist plots of 10-layer CZTS films deposited at 150 °C using different spray distances and measured at (a) −0.3 V and (b) −1.0 V versus RHE.*

3.1.1.2. Twenty-Layer Films

For 20-layer films, the LSV response depended significantly on spray distance (Figure 4). At −0.6 V, Z10 yielded the highest cathodic current density value (~10 mA cm^{-2}), followed by Z40 and Z20 (~9 mA cm^{-2}) and Z30 (~7 mA cm^{-2}), respectively. Therefore, the advantage of Z20 observed in 10L did not persist in 20L. The 20-layer series also produced lower currents compared to the best 10-layer film; this could be due to additional resistance within the film or less homogeneous deposition during repeated deposition, which is consistent with the obtained results.

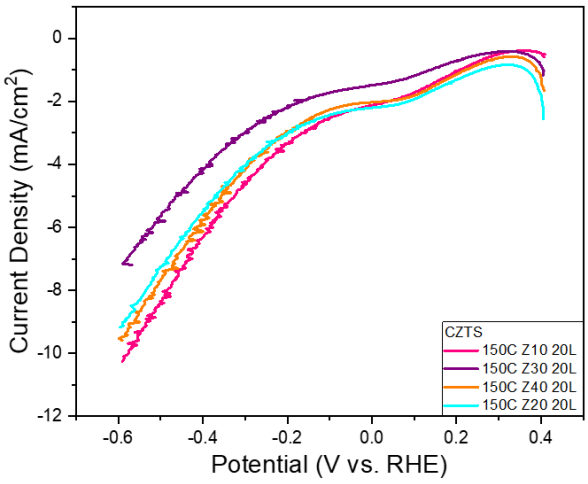


Figure 4. *LSV curves of 20-layer CZTS films deposited at 150 °C using different spray distances.*

The 20-layer Tafel plots are shown in Figure 5. The apparent slopes were 771, 789, 734, and 747 mV dec^{-1} for Z10, Z20, Z30, and Z40, respectively. Z30 yielded the lowest value, and the overall range of 734–789 mV dec^{-1} is narrower than the 713–955 mV dec^{-1} range observed for 10L. The distance yielding the lowest slope was also different from the distance yielding the highest LSV current.

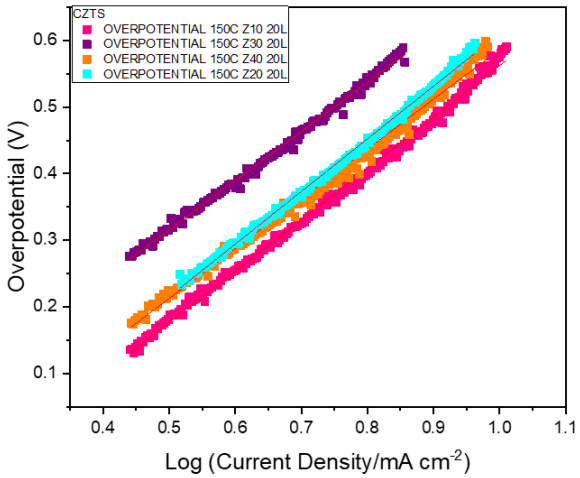


Figure 5. *Tafel plots of 20-layer CZTS films deposited at 150 °C using different spray distances.*

The associated impedance spectrum is presented in Figure 6. At -0.3 V, a set of 20-layer films exhibited resistances that appeared relatively high and close together: approximately 280 Ω for Z10, 300 Ω for Z20, over 300 Ω for Z30, and 300 Ω for Z40. These values were higher than those of a 10-layer series at the same potential. At -1.0 V, the resistance dropped to approximately 40 Ω for Z10, 55 Ω for Z20, 70 Ω for Z30, and 50 Ω for Z40. The lowest impedance and the largest LSV current for this number of layers both occurred in Z10.

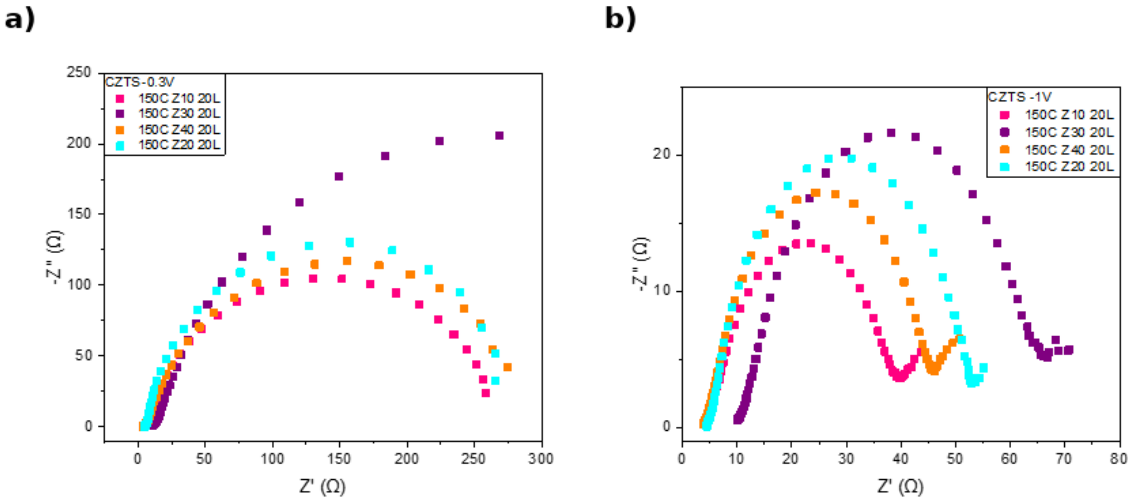


Figure 6. *Nyquist plots of 20-layer CZTS films deposited at 150 °C using different spray distances and measured at (a) −0.3 V and (b) −1.0 V versus RHE.*

3.1.1.3. Thirty-Layer Films

The dependence of 30-layer films on spraying distance was evaluated using the same LSV, Tafel, and EIS measurement sequence, starting with the LSV comparison in Figure 7. At −0.6 V, both Z10 and Z20 generated approximately −12 mA cm^{-2} of current, followed by Z30 with approximately −10 mA cm^{-2} and Z40 with approximately −9 mA cm^{-2}. Therefore, the current decreased with distance beyond Z20. The recovery of Z20 performance at 30L, along with the equally strong response in Z10, suggests that short and medium distances support more effective deposition in the thicker film, while longer distances may result in lower local loading or less homogeneous coating.

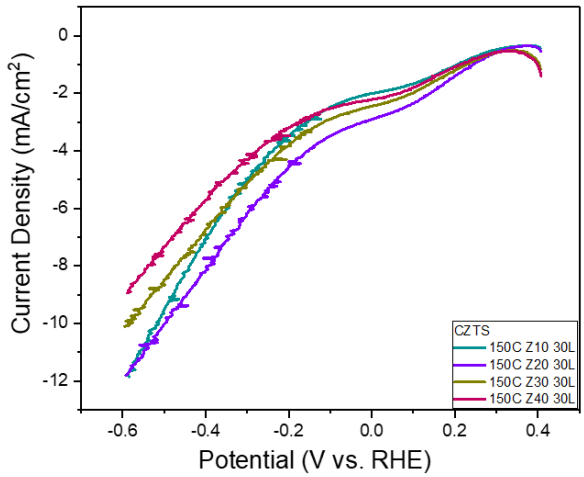


Figure 7. *LSV curves of 30-layer CZTS films deposited at 150 °C using different spray distances.*

Figure 8 compares the corresponding Tafel plots. Z10 clearly shows the lowest apparent slope at 701 mV dec^{-1}; Z20, Z30, and Z40 cluster together in the range of 851–882 mV dec^{-1}. The difference of ≈150 mV dec^{-1} between Z10 and the cluster is clearly above the measurement distribution. The narrow clustering of the latter three curves indicates similar fitted slope behavior, but it does not establish identical intrinsic kinetics.

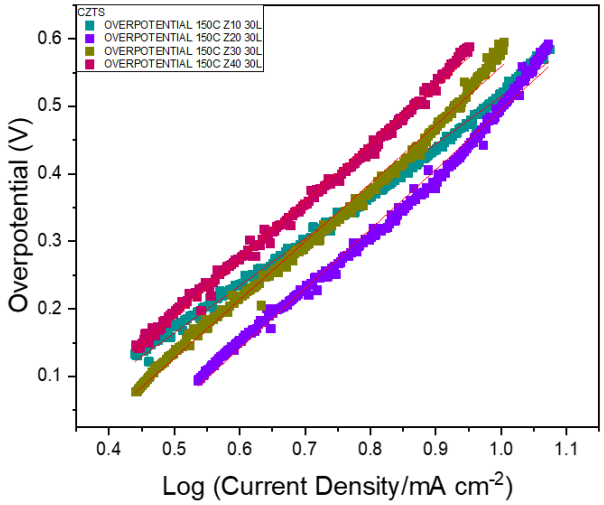


Figure 8. *Tafel plots of 30-layer CZTS films deposited at 150 °C using different spray distances.*

The EIS spectra were shown in Figure 9. At −0.3 V, Z20 gave the lowest apparent Rct (~175 Ω), followed by Z30 (~225 Ω), Z10 (~250 Ω), and Z40 (>275 Ω). At −1.0 V, Z10 and Z20 both gave approximately 35 Ω, while Z40 gave the highest reported value (~55 Ω). The spectra contained more clearly developed arcs than several thinner-film datasets. For the 30-layer series, the LSV and EIS results therefore converged on Z10–Z20 as the preferred distance range, with Z20 giving the lowest low-potential impedance.

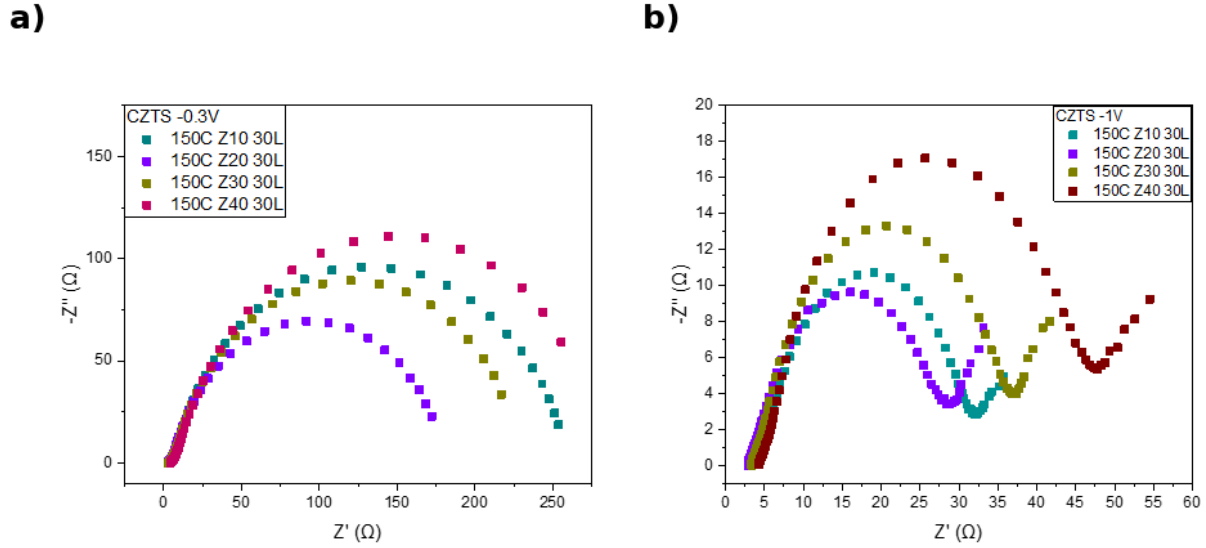


***Figure 9**. Nyquist plots of 30-layer CZTS films deposited at 150 °C using different spray distances and measured at (a) −0.3 V and (b) −1.0 V versus RHE.*

Across the 150 °C series, no single distance minimizes every electrochemical response at every layer number. Z20 maximized LSV current for 10L and performed equally well with Z10 for 30L, whereas Z10 was strongest for 20L. Low-potential EIS showed better results with Z40, Z10, and Z20 for 10L, 20L, and 30L, respectively. The parameter dependence is therefore interactive: changing layer number changes the deposition history and film geometry, which in turn changes the distance that gives the most favorable response.

3.1.2. Spray-Distance Effects at 200 °C

3.1.2.1. Ten-Layer Films

The 200 °C series was used to determine whether the distance dependence changed under a substantially faster evaporation regime. The 10-layer LSV curves are presented in Figure 10. At −0.6 V, Z30 showed approximately −9 mA cm^{-2} and Z40 approximately −8 mA cm^{-2}, whereas Z10 and Z20 showed approximately −7 and −6.5 mA cm^{-2}, respectively. The best distance therefore shifted from Z20 at 150 °C to Z30 at 200 °C for 10-layer films. The longer distance may partially mitigate the extremely rapid drying occurring on the hotter substrate by allowing more droplet cooling or solvent loss before impact. A vapor cushion or Leidenfrost-like interaction may also

reduce deposition efficiency at short distances; however, this remains a hypothesis as droplet impact was not directly observed.

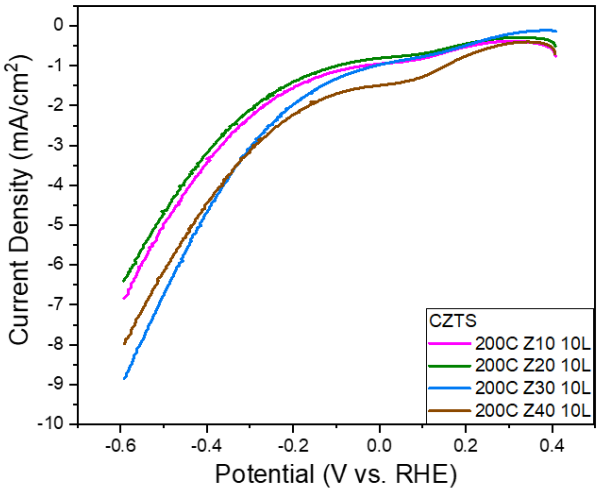


***Figure 10**. LSV curves of 10-layer CZTS films deposited at 200 °C using different spray distances.*

Figure 11 shows the Tafel plots of 10-layer films produced at 200 °C. Z10 and Z20 yielded indistinguishable slopes (619 and 617 mV dec^{-1}1, respectively); Z30 remained close with 641 mV dec^{-1}, while the highest value was measured in Z40 with 731 mV dec^{-1}. The distance-dependent spread in this parameter set is 114 mV dec^{-1}; approximately half the 242 mV dec^{-1} observed in the 150 °C set with the same number of layers; this indicates that the slope calculated at 200 °C is less sensitive to distance. Slopes at 200 °C are generally lower than those obtained from the 150 °C parameter set; for example, Z40 dropped from 955 to 731 mV dec^{-1}.

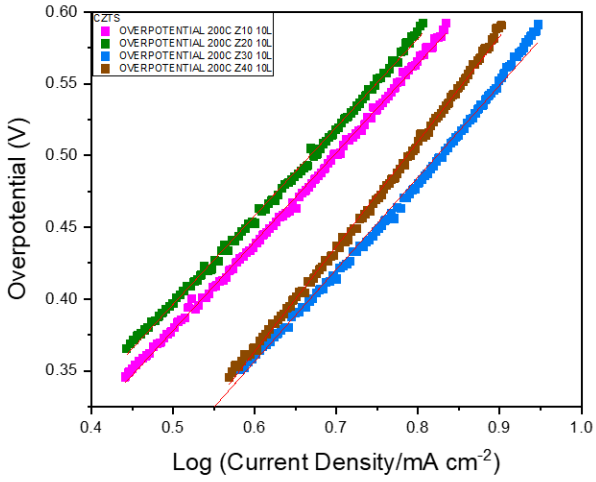


***Figure 11**. Tafel plots of 10-layer CZTS films deposited at 200 °C using different spray distances.*

Figure 12 compares the 200 °C, 10-layer impedance spectra. At −0.3 V, the apparent Rct values were approximately 400 Ω for Z40, 500 Ω for Z30, 700 Ω for Z10, and more than 700 Ω for Z20. These values were approximately two to three times those measured for the 150 °C, 10-layer series (~150–270 Ω). At −1.0 V, the 200 °C values decreased to approximately 55–80 Ω but remained

above the ~30–40 Ω range at 150 °C; Z30 gave the smallest value (~55 Ω), while Z20 showed the largest arc. LSV and high-potential EIS therefore both favored Z30 for this condition.

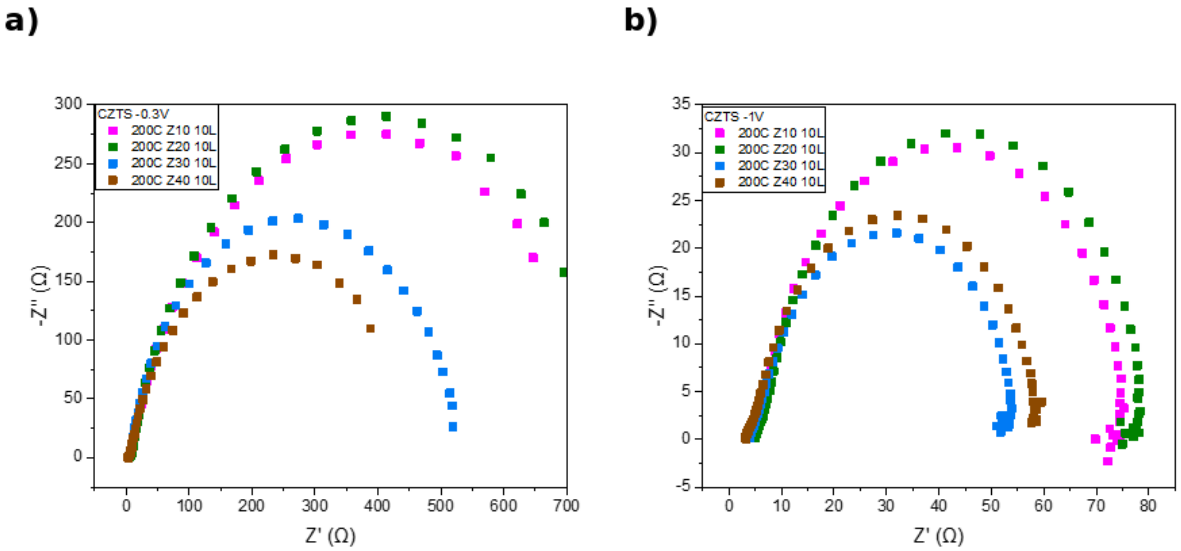


Figure 12. *Nyquist plots of 10-layer CZTS films deposited at 200 °C using different spray distances and measured at (a) −0.3 V and (b) −1.0 V versus RHE.*

3.1.2.2. Twenty-Layer Films

For the 200 °C, 20-layer series, the LSV ranking changed again (Figure 13). At distances Z10 and Z40, the highest cathodic current density was obtained at −0.6 V (~8 mA cm^{-2}), followed by Z30 (~7 mA cm^{-2}) and Z20 (~6.5 mA cm^{-2}). Therefore, Z20 represents the distance that yields the lowest result at this temperature and number of layers; this is the opposite of the behavior in the selected 150 °C, 10-layer configuration. The result shows that the preferred distance is not fixed but depends on both temperature and number of layers.

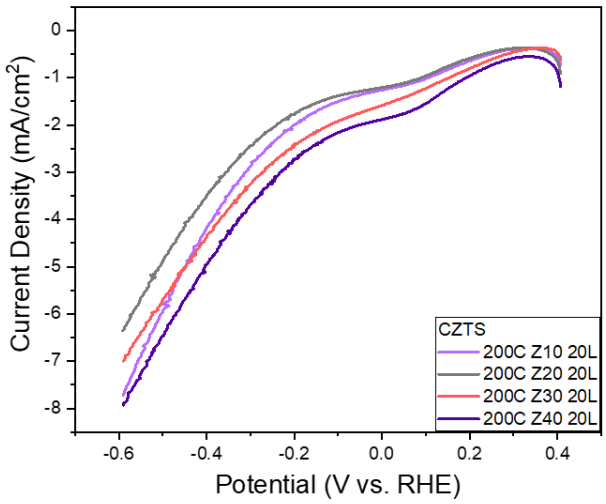


Figure 13. *LSV curves of 20-layer CZTS films deposited at 200 °C using different spray distances.*

Tafel slopes are presented in Figure 14. The slopes are 665 mV dec^{-1} for Z10, 707 mV dec^{-1} for Z20, 866 mV dec^{-1} for Z30, and 865 mV dec^{-1} for Z40. The difference between Z10 and Z40 is 201 mV dec^{-1}. Therefore, shorter distances produce slopes that are smaller, while the largest LSV current is obtained at the shortest and longest distances. This result cannot be resolved by assuming a smaller number of faster sites; the present data do not independently determine site density or site-normalized activity.

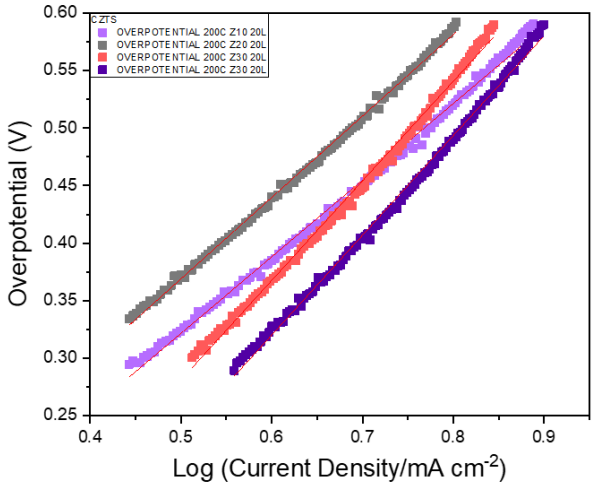


Figure 14. *Tafel plots of 20-layer CZTS films deposited at 200 °C using different spray distances.*

At −0.3 V, Z40 showed approximately 350 Ω and Z30 approximately 400 Ω, while both Z10 and Z20 exceeded 500 Ω. At −1.0 V, Z10, Z30, and Z40 converged near 60 Ω, whereas Z20 remained higher at approximately 75 Ω. Thus, Z20 gave the weakest LSV response and the largest high-potential impedance. Longer distances generally reduced the low-potential impedance at 200 °C, although Z10 and Z40 produced equal LSV currents.

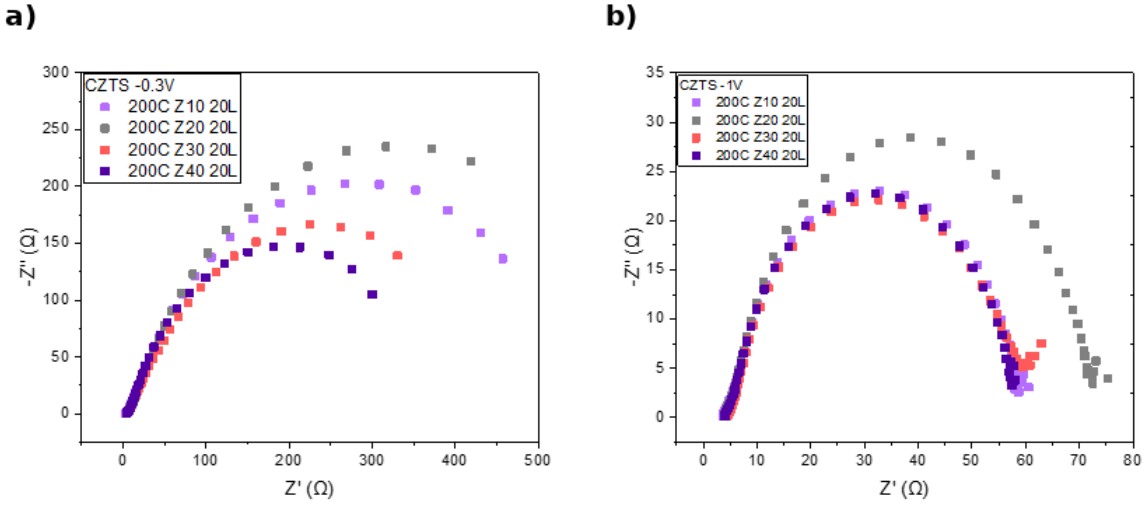


Figure 15. *Nyquist plots of 20-layer CZTS films deposited at 200 °C using different spray distances and measured at (a) −0.3 V and (b) −1.0 V versus RHE.*

3.1.2.3. Thirty-Layer Films

The final distance comparison at 200 °C was performed using 30 layers (Figure 16). At −0.6 V, Z30 showed approximately −8 mA cm^{-2}, Z10 and Z20 approximately −7 mA cm^{-2}, and Z40 approximately −6.5 mA cm^{-2}. Therefore, Z30 gave the strongest response, while Z40 showed the lowest performance in this parameter set. Unlike the 10-layer series, increasing the distance from Z30 to Z40 reduced the electrochemical response; this leads to poor performance for thick films due to the excessive distance. Importantly, Z30 gave the best result for the 10L and 30L parameter sets at 200 °C, but not for 20L; this confirms that the temperature-distance interaction is layer-dependent.

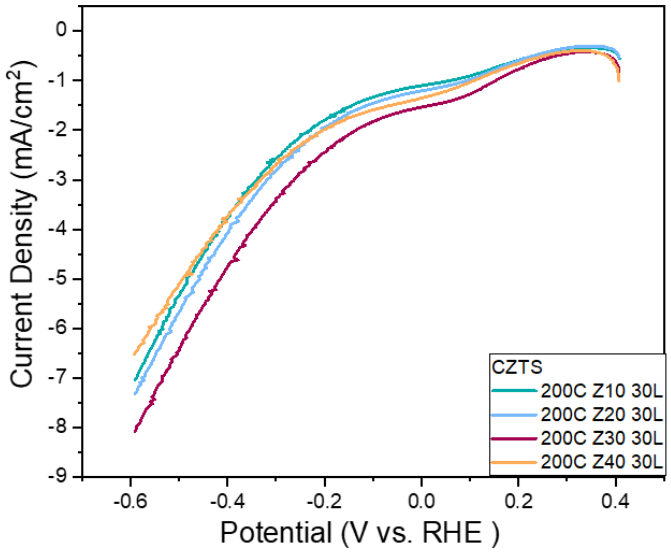


Figure 16. *LSV curves of 30-layer CZTS films deposited at 200 °C using different spray distances.*

The corresponding apparent Tafel slopes are compared in Figure 17. The slopes for this parameter set are 664, 689, 767, and 753 mV dec^{-1} for Z10, Z20, Z30, and Z40, respectively. Z10 again gives the lowest slope, while Z20 is the other parameter with the lowest value. The 664–767 mV dec^{-1} range is narrower than the 656–867 mV dec^{-1} range of the 20-layer series; this indicates that the adapted slope becomes less sensitive to distance in the 30-layer series. The lowest slope nevertheless remained associated with Z10 rather than the LSV optimum at Z30.

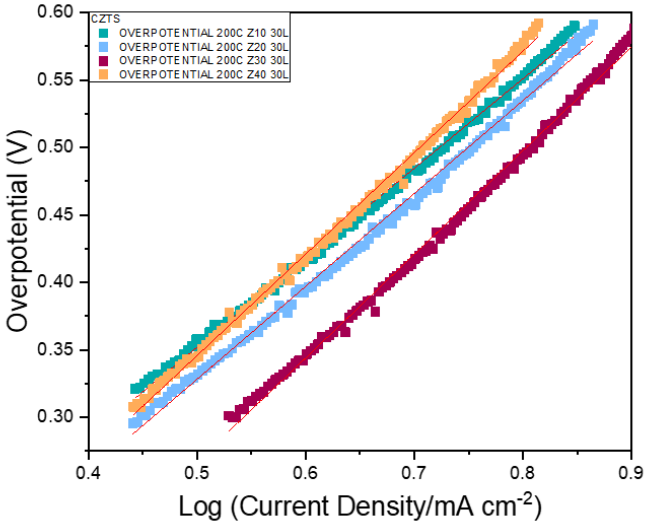


Figure 17. *Tafel plots of 30-layer CZTS films deposited at 200 °C using different spray distances.*

At −0.3 V, Z30 showed the lowest Rct (~450 Ω), while Z10, Z20, and Z40 all exceeded 600 Ω (Figure 18). At −1.0 V, Z30 again showed the smallest value (~55 Ω), whereas Z40 gave the largest (~75 Ω). The agreement between LSV and EIS identifies Z30 as the preferred distance for 30-layer films at 200 °C.

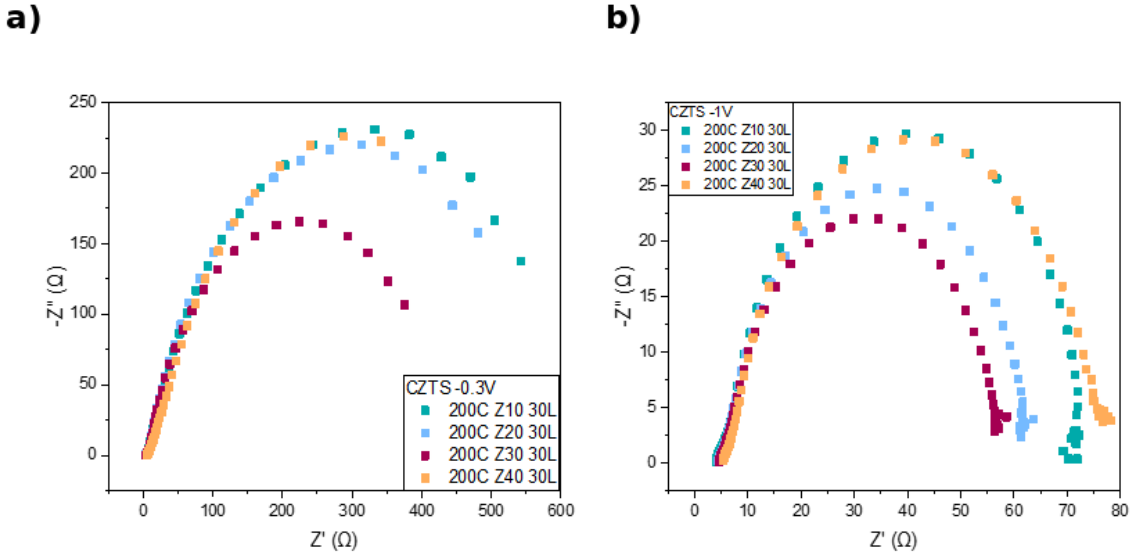


Figure 18. *Nyquist plots of 30-layer CZTS films deposited at 200 °C using different spray distances and measured at (a) −0.3 V and (b) −1.0 V versus RHE.*

3.1.3. Influence of Layer Number at 150 °C and Z20

After examining the samples prepared according to the distance, the number of layers deposited at the optimum Z20 and 150 °C was directly compared. The number of layers controls the amount of catalyst applied and contributes to the resulting film thickness. Therefore, as shown in Figure 19, films containing 5, 10, 20, and 30 layers were evaluated, with all other conditions being the same. The cathodic current densities at −0.6 V were approximately −11, −14, −9, and −12 mA cm^{-2} for 5L, 10L, 20L, and 30L, respectively. The results were ranked as 10L > 30L > 5L > 20L. Therefore, increasing the number of layers did not provide a monotonic improvement. Ten layers provided sufficient catalytic material while maintaining adequate electrical and ionic conductivity, whereas the lower response of the 20-layer film suggests that the added material may also increase resistance or deposition heterogeneity. The partial improvement at 30 layers demonstrates that the number of layers is not merely an indicator of activity but rather interacts with the detailed film structure.

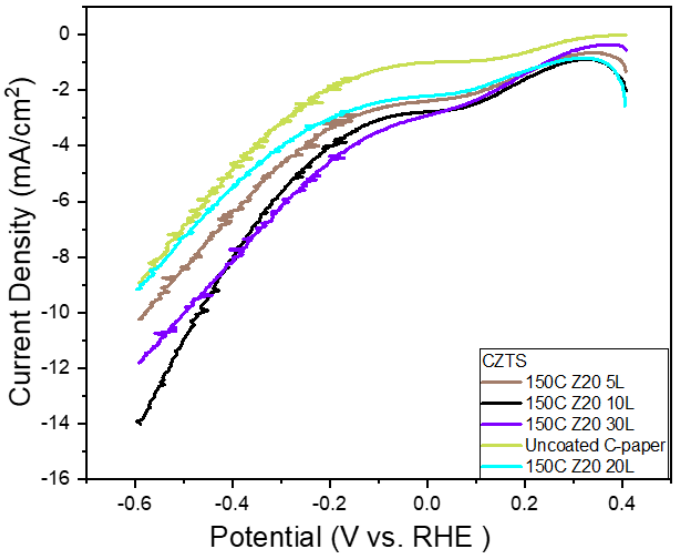


Figure 19. *LSV curves of CZTS films containing different numbers of layers and deposited at 150 °C and Z20.*

Tafel plots are compared in Figure 20. The slopes were 776 mV dec^{-1} for 5L, 754 mV dec^{-1} for 10L, 789 mV dec^{-1} for 20L, and 882 mV dec^{-1} for 30L. The slope is not monotonic: 10L gave the lowest slope, while 30L gave the highest slope. The smaller slope of the ten-layer film should not be directly attributed to inherently faster regions at higher densities, as the Tafel slope alone measures neither region density nor conversion frequency. Instead, it indicates that the current of this film increased more steeply with overpotential within the chosen fit range.

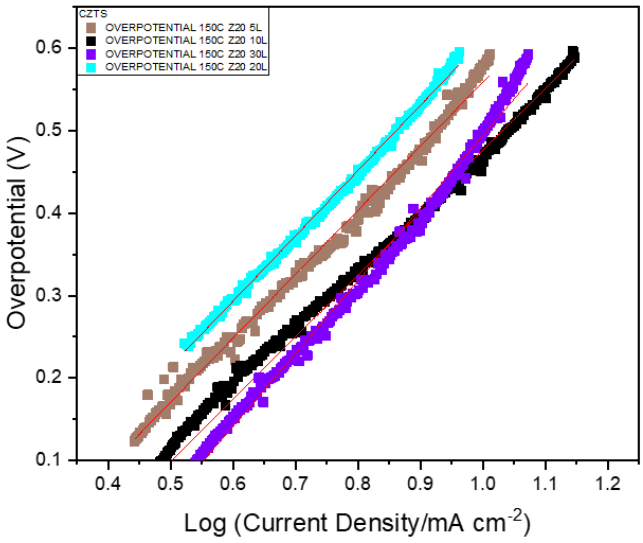


Figure 20. *Tafel plots of CZTS films containing different numbers of layers and deposited at 150 °C and Z20.*

EIS provides an additional comparison of the layer-number series (Figure 21). At −0.3 V, the Rct values were approximately 225 Ω for 5L, 200 Ω for 10L, more than 250 Ω for 20L, and 175 Ω for 30L; uncoated carbon paper also showed a value above 250 Ω. At −1.0 V, the corresponding values decreased to nearly 45, 35, 55, and 30 Ω. Therefore, while 30L showed better activity in the EIS results, LSV 10L also yielded better results. The 20-layer sample showed both the lowest LSV current among the coated films and the largest coated-film impedance at both potentials, providing consistent evidence of negative transport in that particular film. Because the optimization goal was maximum cathodic current rather than minimum impedance alone, 10L was selected as the optimum layer number.

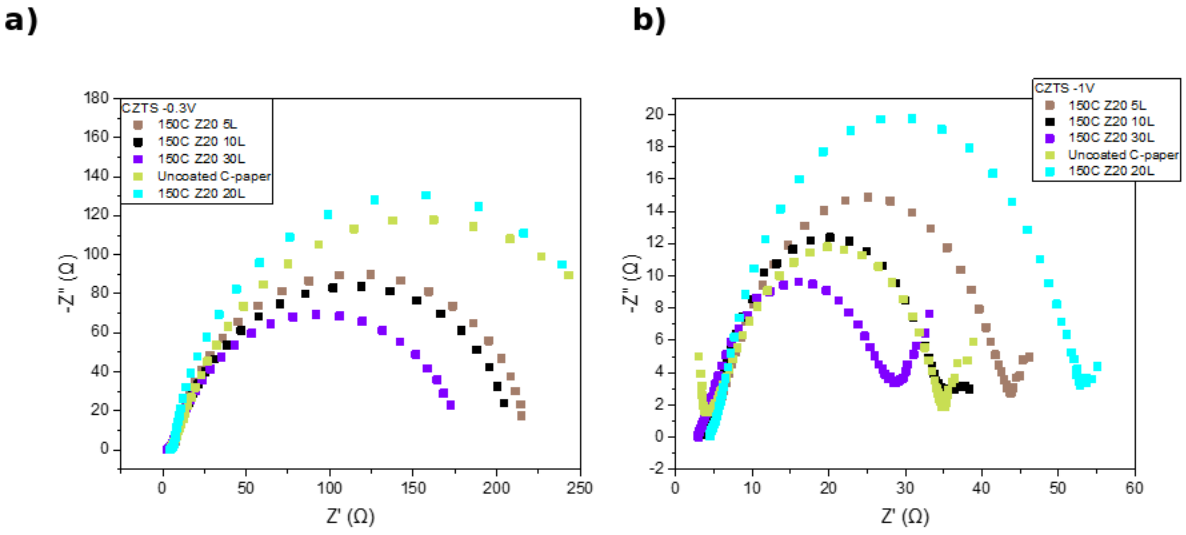


Figure 21. *Nyquist plots of CZTS films containing different numbers of layers and deposited at 150 °C and Z20, measured at (a) −0.3 V and (b) −1.0 V versus RHE.*

3.1.4. Platform-Temperature Comparison and Integrated Optimization

The direct temperature comparison was considered after the distance- and layer-dependent datasets so that temperature could be interpreted as the higher-level film-formation variable. Platform temperature controls solvent evaporation during ultrasonic spray coating and therefore influences droplet drying, nanoparticle rearrangement, film continuity, porosity, and adhesion. The solvent used in the ink, isopropanol (IPA), has a boiling point of 82.4 °C. Although the investigated temperatures of 100, 150, and 200 °C all exceeded this value, their different evaporation rates were expected to produce different film-formation regimes. The temperature effect was isolated using the common Z20–10L configuration.

The LSV curves obtained for the three platform temperatures are compared in Figure 22. A clearly non-monotonic temperature dependence was observed. According to RHE, the film prepared at -0.6 V and 150 °C yielded the highest current density of approximately 14 mA cm^{-2}; this value is higher than approximately 9 mA cm^{-2} at 100 °C and 6.5 mA cm^{-2} at 200 °C. The 150 °C curve also shows the highest increase in cathodic current as the potential becomes more negative. Therefore, the activity is 150 °C >100 °C >200 °C, and the 150 °C sample shows the highest current density measured in the entire CZTS dataset. This trend is related to the balance between solvent removal and nanoparticle organization during drying. At 100 °C, relatively slow evaporation can prolong drying time between each pass and limit the formation of effective interparticle contacts. At 150 °C, solvent removal is likely sufficiently rapid, but still allows for droplet spreading and particle rearrangement, supporting the formation of a continuous and well-adhered film. At 200 °C, very rapid evaporation can immobilize particles before proper packing is achieved and create capillary or thermal stresses that increase porosity, cracking, or interfacial discontinuities. These explanations remain mechanistic interpretations of the electrochemical trends and would require direct morphological evidence for confirmation.

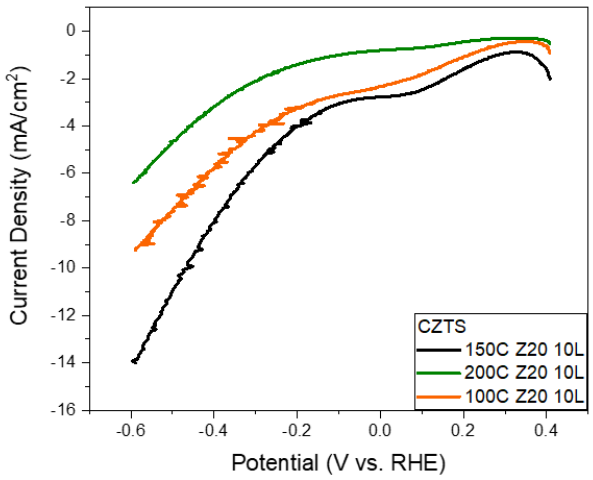


Figure 22. *LSV curves of Z20–10L CZTS films prepared at platform temperatures of 100, 150, and 200 °C.*

Tafel analysis was then used to compare the potential dependence of the cathodic current (Figure 23). Linear fitting of the selected regions yielded slopes of 842, 754, and 617 mV dec^{-1} for the 100, 150, and 200 °C samples, respectively. The value at 200 °C was approximately 27% lower than the value at 100 °C. Within the appropriate range, a smaller slope implies that a smaller additional overpotential is needed to increase the current tenfold. However, the location of the full Tafel analysis must also be considered. The 150 °C curve lies at a lower overpotential than the 200 °C curve within the shared current density range; this is consistent with the larger absolute current observed with LSV. Thus, the lower slope of the 200 °C sample does not indicate better overall HER performance.

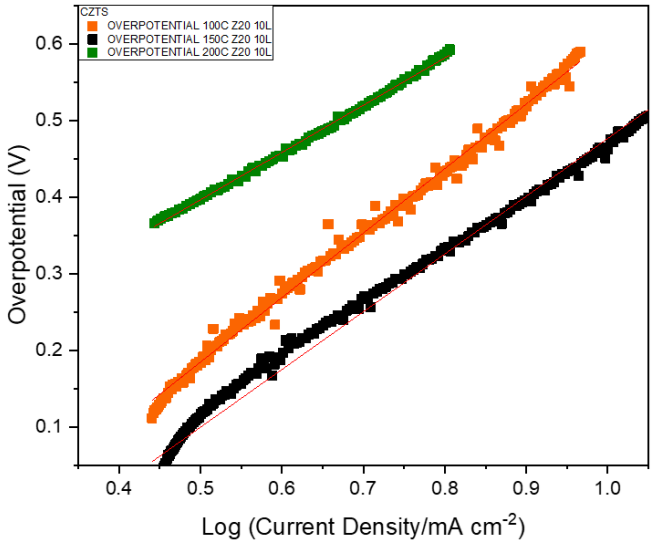


Figure 23. *Tafel plots of Z20–10L CZTS films prepared at 100, 150, and 200 °C.*

All Tafel slopes measured in the broader parameter study ranged from 617 to 955 mV dec^{-1}, substantially exceeding the ideal value of approximately 120 mV dec^{-1}, often associated with a Volmer-limited HER at room temperature.(Shinagawa, Garcia-Esparza and Takanabe, 2015) Assignment of a rate-determining elementary step from these values is therefore not justified. In neutral 0.5 M Na_2SO_4, water dissociation can introduce an additional kinetic barrier because the proton concentration is low (Lasia, 2019). Uncompensated ohmic resistance, restricted transport through the nanoparticle film, hydrogen-bubble coverage, and mass-transfer limitations at high overpotential may further increase the measured slopes (Raveendran, Chandran and Dhanusuraman, 2023; Wan *et al.*, 2024). Therefore, slopes are only used for experimental comparison within equivalent measurement conditions.

EIS was measured at −0.3 and −1.0 V to compare the impedance response at two operating potentials (Figure 24). At -0.3 V, Rct was lowest for the 150 °C sample (~200 Ω), moderate for the 100 °C sample (~250 Ω), and highest for the 200 °C sample (>275 Ω). Since low-frequency intercepts are not fully resolved, these values should be considered approximate. Nevertheless, the ranking agrees with the LSV results and indicates that the 150 °C film provided the most favorable interfacial and through-film charge-transfer pathway at low driving force.

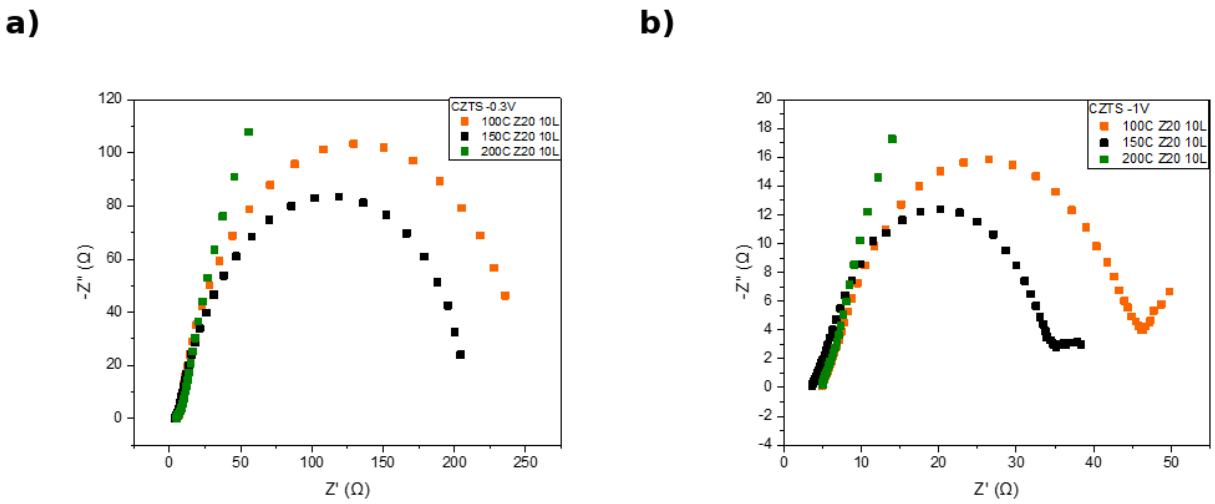


Figure 24. *Nyquist plots of Z20–10L CZTS films prepared at different platform temperatures and measured at (a) −0.3 V and (b) −1.0 V versus RHE.*

At −1.0 V, the resistance decreased to approximately 35 Ω at 150 °C, 50 Ω at 100 °C, and more than 50 Ω at 200 °C. The 100 °C spectrum contained two recognizable arcs, indicating at least two resolved time constants; without equivalent-circuit analysis, these features cannot be attributed uniquely to charge transfer and mass transport. The 200 °C spectrum remained relatively wide and incomplete. When the LSV and EIS results are considered together, they indicate that the optimal platform temperature in the studied range is 150 °C, while the smaller-appearing Tafel slope at 200 °C reflects a fitted curve shape rather than superior absolute activity.

Table 4 summarizes the distance giving the strongest response for each descriptor and makes the interaction between variables explicit. At −0.3 V, every 200 °C film showed higher impedance than its 150 °C counterpart across the investigated distances and layer numbers. At −1.0 V, the same general trend remained, with one reported exception, while the 150 °C values were mostly within 30–70 Ω. Within the 150 °C series, the lowest low-potential Rct values were approximately 150 Ω for 10L at Z40 and 175 Ω for 30L at Z20; the 20-layer values were comparatively insensitive to distance at approximately 280–300 Ω or higher.

Table 4. *Distance giving the strongest response for each electrochemical descriptor.*

Condition	Largest |j| at −0.6 V	Lowest apparent Tafel slope	Lowest Rct at −0.3 V	Lowest Rct at −1.0 V
150 °C, 10L	Z20 (~14 mA cm^{-2})	Z10 (713 mV dec^{-1})	Z40 (~150 Ω)	All ~30–40 Ω
150 °C, 20L	Z10 (~10 mA cm^{-2})	Z30 (734 mV dec^{-1})	Z10 (~280 Ω)	Z10 (~40 Ω)
150 °C, 30L	Z10/Z20 (~12 mA cm^{-2})	Z10 (701 mV dec^{-1})	Z20 (~175 Ω)	Z10/Z20 (~35 Ω)
200 °C, 10L	Z30 (~9 mA cm^{-2})	Z20 (617 mV dec^{-1})	Z40 (~400 Ω)	Z30 (~55 Ω)
200 °C, 20L	Z10/Z40 (~8 mA cm^{-2})	Z10 (665 mV dec^{-1})	Z40 (~350 Ω)	Z10/Z30/Z40 (~55 Ω)
200 °C, 30L	Z30 (~8 mA cm^{-2})	Z10 (664 mV dec^{-1})	Z30 (~450 Ω)	Z30 (~55 Ω)

Overall, the complete dataset supports three conclusions. Firstly, 150 °C is preferred over 200 °C because it produces the maximum LSV current and consistently lower impedance. Secondly, the preferred distance varies with the number of layers and temperature, so the distance cannot be optimized independently. Thirdly, the smallest apparent Tafel slope frequently occurred in a sample that did not yield the largest absolute current; this confirms that the slope, curve position, accessible area, and impedance should be considered together. On this combined basis, 150 °C, Z20, and 10L were retained as the optimum CZTS coating parameters because this configuration delivered the largest cathodic current density (~ −14 mA cm^{-2}) while maintaining comparatively low impedance.

3.1.5. Photoelectrochemical Response and Stability of the Optimum CZTS Film

The optimized CZTS film (150 °C, Z20, 10L) was subsequently examined under dark and illuminated conditions in neutral and acidic electrolytes. LSV was used to assess the steady polarization response, chopped-light chronoamperometry (CA) to quantify the reproducible photocurrent, and chronopotentiometry (CP) to evaluate the potential required to sustain a constant cathodic current over extended operation.

Figure 25 compares dark and illuminated LSV curves in neutral and acidic media. At −0.6 V versus RHE, the neutral electrolyte produced approximately −14 mA cm^{-2} in the dark and −13.5 mA cm^{-2} under illumination. The small reduction in current magnitude under light indicates that positive steady-state photoenhancement is not resolved under this condition.

In the acidic electrolyte, the corresponding current densities were approximately −0.10 mA cm^{-2} in the dark and −0.13 mA cm^{-2} under illumination, revealing a small but measurable light-induced enhancement. The much larger absolute current in neutral electrolyte cannot be explained by proton availability and suggests that interfacial stability, surface chemistry, adsorption, electrolyte composition, or charge-transfer pathways strongly influence the response.

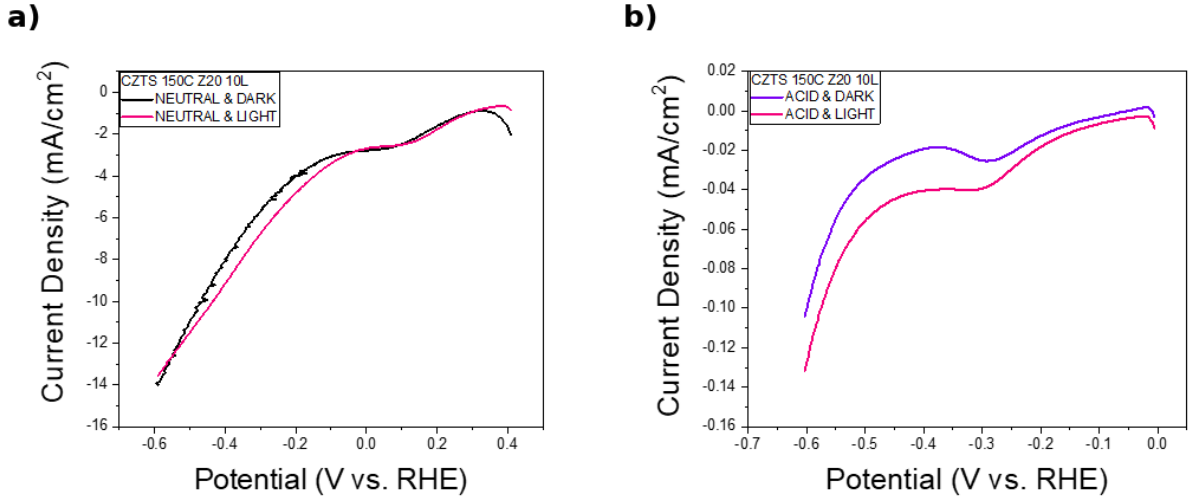


Figure 25. *Dark and illuminated LSV curves of the optimized CZTS film in (a) neutral and (b) acidic electrolyte.*

The transient photoresponse of the optimized CZTS film was evaluated by chopped-light chronoamperometry with 30 s dark–30 s light cycles, performed in 0.5 M Na_2SO_4 at −0.6 V and in 0.5 M H_2SO_4 at −0.2 V vs. RHE (Figure 26). Synchronized periodic current oscillations with the

intermittent illumination were observed in both electrolytes, persisting after an initial transient and demonstrating a reproducible photoresponse. The early baseline evolution consists of interfacial charging and conditioning after application of the constant potential; it should not be assigned uniquely to contaminant removal without additional surface analysis. The photocurrent magnitude was approximately 0.14 mA in the neutral electrolyte and 2.5 µA in the acidic electrolyte; this corresponds to an approximately 56-fold increase in the neutral environment. While a higher proton concentration would normally facilitate proton reduction, the suppressed acidic photocurrent indicates that the reaction is primarily controlled by charge dissociation and transfer at the interface rather than proton supply. Acid-induced surface modification or additional carrier trapping may contribute, while ionic strength, anion adsorption, and differing reaction kinetics may also influence the comparison. The chopped-light amplitudes and the steady LSV light–dark differences were obtained using different protocols and should therefore not be equated directly.

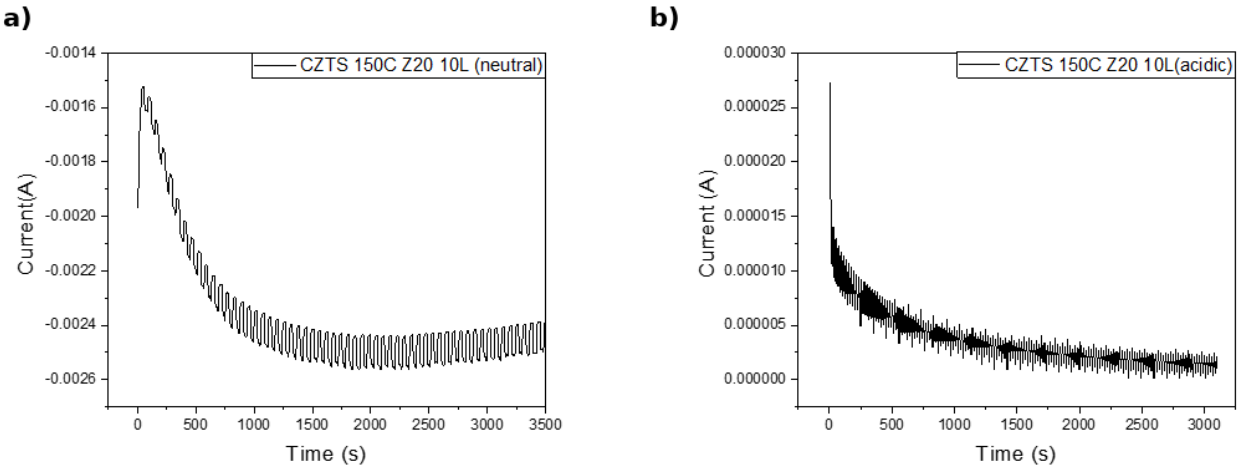


Figure 26. *Chopped-light chronoamperometry of the optimized CZTS film in (a) 0.5 M Na_2SO_4 at −0.6 V and (b) 0.5 M H_2SO_4 at −0.2 V versus RHE.*

Operational behavior was finally examined by CP in neutral electrolyte at -0.6V vs RHE (Figure 27). The measurement extended for approximately 13,000 s (~3.6 h). During the initial 0–3,000 s transient, the potential began near −0.14 V versus RHE, shifted to a maximum of approximately −0.10 V after about 1,000–1,500 s, and then moved progressively to more negative values. The largest change occurred before approximately 5,000–6,000 s. After ~6,000 s, the potential approached a plateau near −0.28 V and remained close to this value until the end of the test. The difference between the transient maximum (~−0.10 V) and the final plateau was approximately 180 mV.

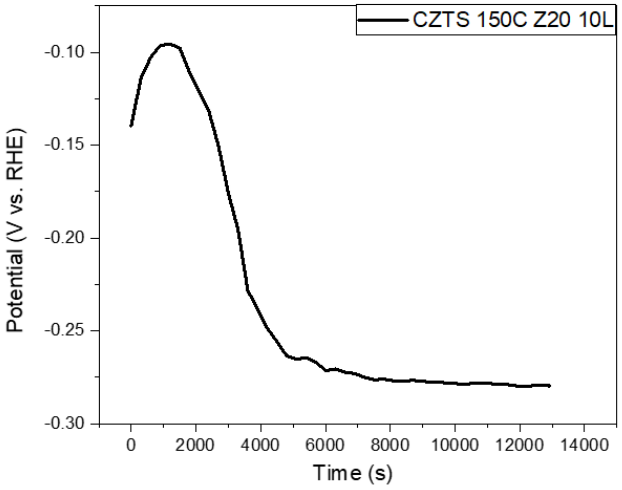


Figure 27. *Chronopotentiometric response of the optimized CZTS film in 0.5 M Na_2SO_4 (pH 7) under constant cathodic current for approximately 13,000 s.*

The initial potential evolution indicates substantial electrode conditioning and/or a change in the electrode–electrolyte interface before steady operation was established. The later plateau shows that the potential required to maintain the imposed current became comparatively stable for the final ~7,000 s. The experiment therefore supports short-term operational stability after an initial conditioning period, rather than complete invariance over the full 3.6 h. Verification of long-term stability will also require repeated electrode testing, post-test characterization, and comparison of pre- and post-operation activity.

3.2. Cobalt Selenide (CoSe)

This section will examine the effects of spraying distance and then the number of layers on CoSe coatings, and the electrochemical techniques used for each parameter set (CV, LSV, EIS, Tafel, and ECSA) will be discussed in detail. Tested only at 150 °C and in an acidic electrolyte (0.5 M H_2SO_4, pH 0).

3.2.1. Influence of Distance

Cathodic current densities measured at a potential of -0.6 V vs. RHE were obtained as follows: ~ −45 mA/cm^2 for Z10, ~ −140 mA/cm^2 for Z20, ~ −35 mA/cm^2 for Z30, and ~ −35 mA/cm^2 for Z40 (Figure 28). The highest performance was clearly shown by the Z20 parameter (~ −140 mA/cm^2). According to the results, CoSe is extremely sensitive to spraying distance. The Z20 parameter shows approximately 3-4 times higher performance compared to other distances. While the Z30 and Z40 distances showed almost the same performance (~ −35 mA/cm^2), the Z10 distance exhibited a slightly higher value (~ −45 mA/cm^2). This high performance demonstrates that it covers a 1 cm^2 area in the most homogeneous manner, provides the best particle-substrate contact, and creates the optimum spray geometry.

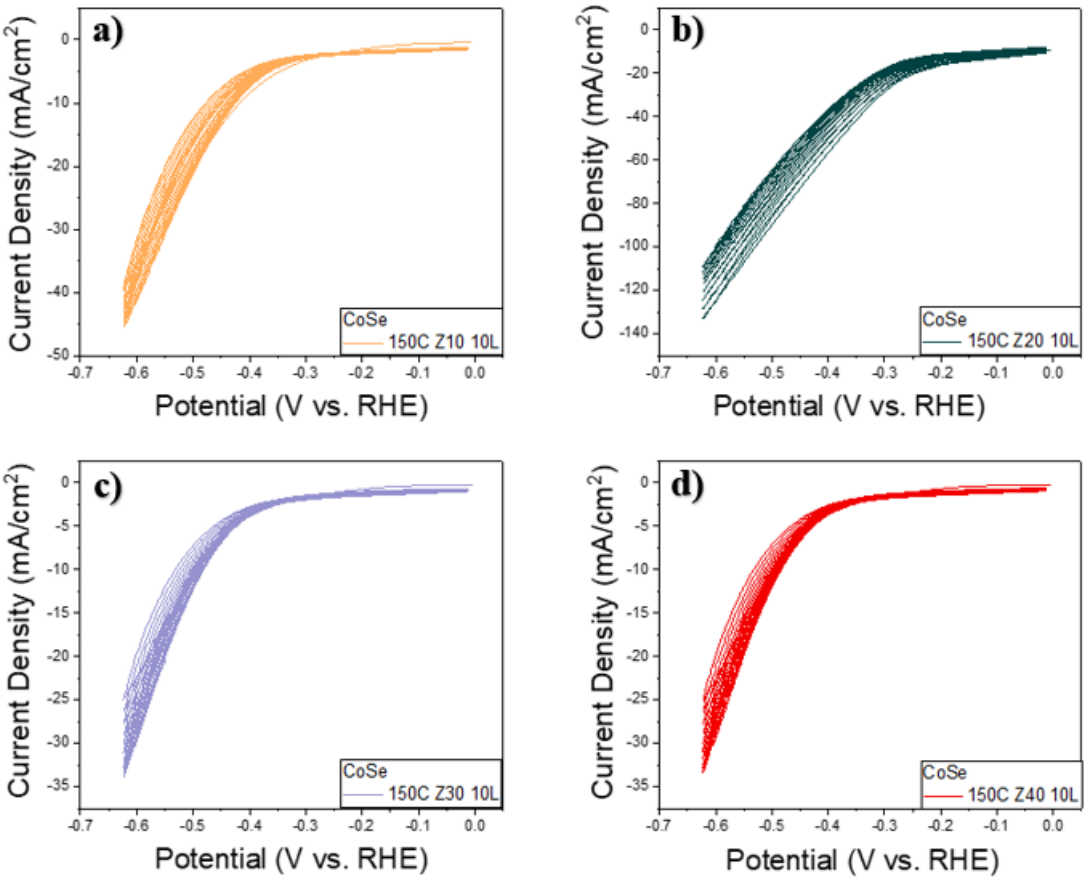


Figure 28. *CV of CoSe films coated (150 °C, 10 L) with different distances from a)10 mm, b)20 mm, c)30 mm and d)40 mm.*

The cathodic current densities measured at a potential of -0.6 V (RHE) were obtained as follows: ~ −40 mA/cm^2 for Z10, ~ −115 mA/cm^2 for Z20, ~ −30 mA/cm^2 for Z30, and ~ −30 mA/cm^2 for Z40 (Figure 29). Accordingly, the performance ranking is Z20 >> Z10 > Z30 ≈ Z40, with the highest current being obtained by a wide margin at the Z20 distance (~ −115 mA/cm^2). The fact that Z30 and Z40 distances yield almost identical performance indicates that surface quality may decrease when sprayed from a certain distance. This behavior shows that distance sensitivity only finds an optimum balance at the Z20 distance, and performance rapidly decreases when moving away from this optimum point.

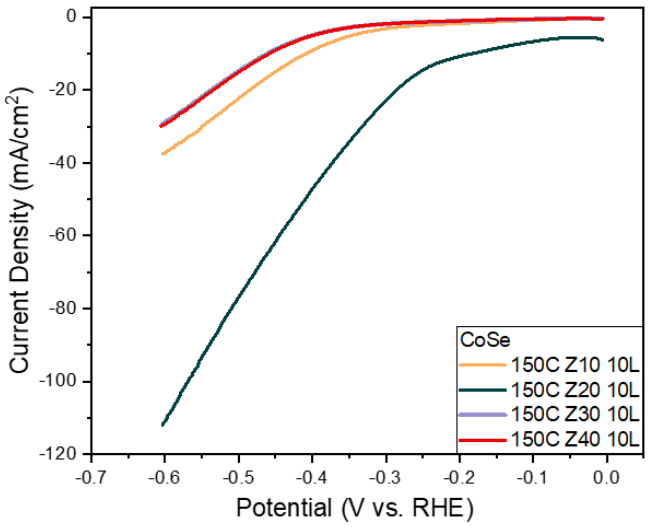


Figure 29. *LSV Results for Distance Comparison (CoSe 150C 10L)*

The values obtained from the Tafel slope analysis are as follows: 260 mV/dec for Z10, 387 mV/dec for Z20, 236 mV/dec for Z30, and 240 mV/dec for Z40 (Figure 30). The lowest slopes were obtained at distances Z30 (236 mV/dec) and Z40 (240 mV/dec), while the highest slope was measured at distance Z20 (387 mV/dec). The Tafel slope reflects the kinetic velocity per unit overvoltage, i.e., how fast a single active region operates; the total current depends on both the kinetics per region and the total number of active regions on the surface. The low Tafel slopes at distances Z30 and Z40 indicate that the small number of active regions in these films operate quickly per region; however, since the total number of active regions is limited (correlated with low CV/LSV current results), the total current remains low.

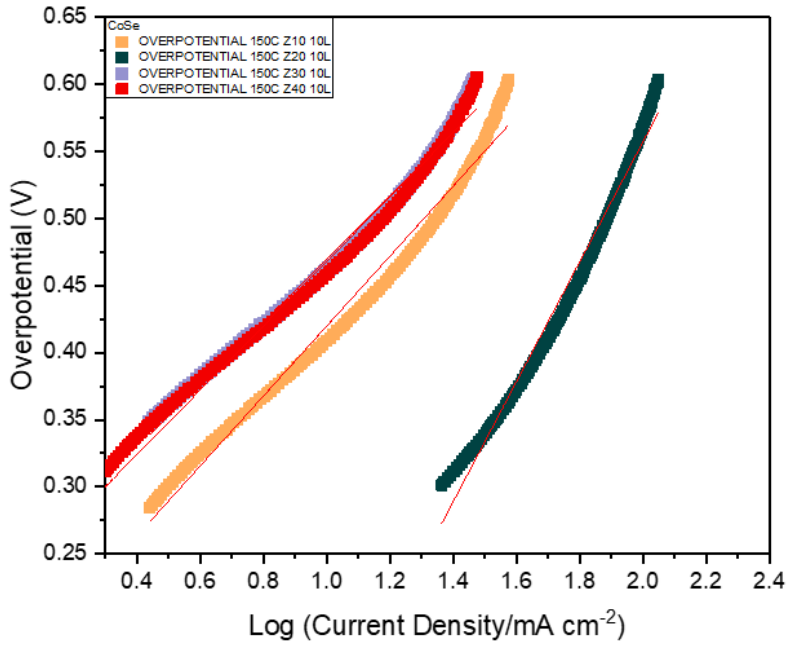


Figure 30. *Tafel Slope Analysis for Distance Comparison (CoSe 150 °C 10 L)*

Electrochemical impedance spectroscopy measurements were performed at three different voltages (−0.2 V, −0.4 V, and −0.5 V). At the low voltage (−0.2 V), the Z20 distance exhibited the lowest charge transfer resistance (~100 Ω), while the other distances yielded much higher resistances: ~900 Ω for Z10, ~1000 Ω for Z40, and ~1100 Ω for Z30 (Figure 31a). Accordingly, Z20 has approximately 9-11 times lower Rct than the other distances. The Z10, Z30, and Z40 distances formed large, complete semicircles with high Rct values. This difference indicates that the Z20 film has a much better electron conduction network and electrode-electrolyte interface. At -0.4 V, the charge transfer resistances decreased significantly for all distances: Z20 showed the lowest Rct (~50 Ω), while Z10 yielded ~275 Ω, and Z30 and Z40 showed ~370 Ω (Figure 31b). At this potential, Z20 provides approximately 6-7 times lower resistance compared to other distances. At -0.5 V, all Rct values decreased by approximately 10-16 times compared to -0.2 V. At this potential, Z20 continued to show the best performance, providing the lowest resistance (~10 Ω), while Z10 gave ~55 Ω, and Z30 and Z40 gave incomplete semicircles (>60 Ω). The order is Z20 >> Z10 > Z30 ~ Z40 (Figure 31c). The fact that Z30 and Z40 distances yield incomplete curves even at high overvoltages indicates that the films at these distances have poor charge transfer properties. The Z20 distance giving the lowest Rct at every potential indicates that the homogeneous and well-bonded film structure provided by this distance creates a low-resistance charge transfer interface. The high Rct values at other distances can be explained by poor particle coupling and insufficient active surface or inadequate coating quality in these films.

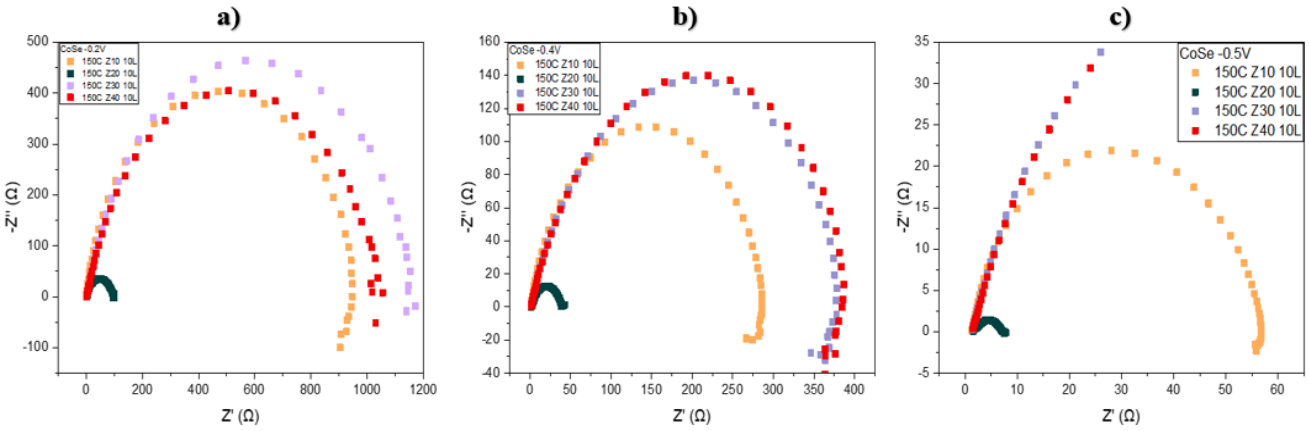


Figure 31. *EIS Results for Distance Comparison (CoSe 150 °C 10 L) at a) -0.2 V, b) -0.4 V, and c) -0.5 V*

Table 5. *ECSA Results for Distance Comparison (CoSe 150C 10L)*

PARAMETERS	ECSA (F/cm^2)
Z10 10L	0.13
Z20 10L	1.41
Z30 10L	0.29
Z40 10L	0.35

ECSA was measured using the double-layer capacitance (C_{dl}) method. For this purpose, CV measurements were taken at different scan rates (50–250 mV/s) in a non-Faradaic potential area (approximately 0.14 V vs RHE). Multicycle scanning (30 cycles) was used for the measurement, and only the last cycle was selected. The first cycles are specifically for equilibrating the electrode surface, cleaning the surface, and ensuring proper wetting; therefore, the most stable results are obtained from the last cycle. The reason for specifically using 0.14 V for capacitive current reading is that the region where the current is almost parallel to the potential is the ideal region for this reading. The data calculated in this way are as follows: 0.13 F/cm^2 for Z10, 1.41 F/cm^2 for Z20, 0.29 F/cm^2 for Z30, and 0.35 F/cm^2 for Z40. Accordingly, the Z20 distance (1.41 F/cm^2) provided the highest active surface area by far, this value being approximately 4-11 times higher than other distances. There is a strong correlation between the catalytic performance of CeSo and the active surface area: the distance that gives the highest current, the lowest charge transfer resistance, and the highest ECSA is the same (Z20). The Z20 parameter provides the optimum geometry, covering the 1 cm^2 area most homogeneously and creating the most accessible active surface area; while insufficient or irregular accumulation at other distances significantly limits the active surface area. Thus, ECSA findings consistently confirm that Z20 is the optimal distance for CoSe using four different techniques (CV, LSV, EIS, ECSA).

3.2.2. Influence of Coating Layers

Cathodic current densities measured at a potential of -0.6 V (RHE) were obtained as follows: ~ −140 mA/cm^2 for 10L, ~ −120 mA/cm^2 for 20L, ~ −130 mA/cm^2 for 40L, ~ −165 mA/cm^2 for 80L, ~ −165 mA/cm^2 for 120L, ~ −175 mA/cm^2 for 160L, and ~ −200 mA/cm^2 for 200L (Figure 32). Accordingly, the highest performance was exhibited by the 200-layer film (~ −200 mA/cm^2).

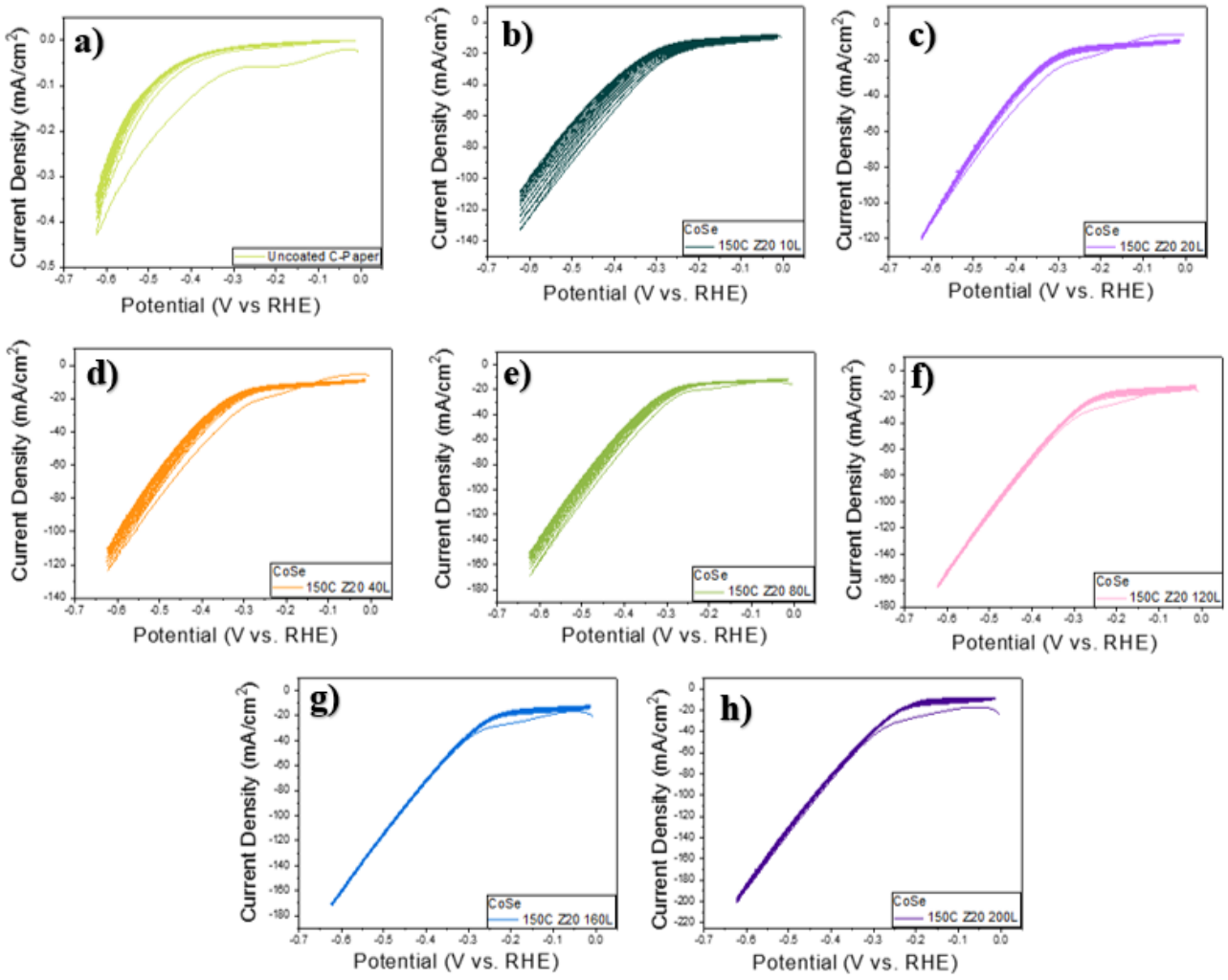


Figure 32. *CV Results of a) Uncoated C-paper and CoSe Films (150 °C, Z20) coated with b) 10 layers, c) 20 layers, d) 40 layers, e) 80 layers, f) 120 layers, g) 160 layers, and h) 200 layers*

The current density increases steadily as the number of layers increases. Only in the 20-layer film is a slight decrease observed compared to the 10-layer film, but the performance recovers and continues to increase at higher layer numbers. This monotonic increasing trend indicates that each additional layer positively contributes to the catalytic performance. The catalytic power of CoSe becomes even more pronounced when compared to uncoated carbon paper. Compared to the negligible current (~ −0.45 mA/cm²) provided by uncoated carbon paper in an acidic environment, the ~ −200 mA/cm² current provided by the 200-layer sample of CoSe corresponds to an approximately 445x catalytic improvement compared to the bare substrate. The important

difference clearly demonstrates that cobalt selenide is an effective hydrogen formation catalyst in an acidic environment and that the measured catalytic activity clearly originates from the catalyst coating.

The effect of the number of layers was also evaluated with LSV, and the monotonic increasing trend, except for 40L observed in CV, was confirmed with this technique, which is LSV (Figure 33). Cathodic current densities measured at a potential of −0.6 V (RHE) at the Z20 distance were obtained as follows: ~ −115 mA/cm^2 for 10L, ~ −115 mA/cm^2 for 20L, ~ −110 mA/cm^2 for 40L, ~ −150 mA/cm^2 for 80L, ~ −160 mA/cm^2 for 120L, ~ −165 mA/cm^2 for 160L, and ~ −190 mA/cm^2 for 200L. Accordingly, the performance ranking is 200L > 160L > 120L > 80L > 10L ≈ 20L > 40L, with the highest current yielded by the 200-layer film (~ −190 mA/cm²).

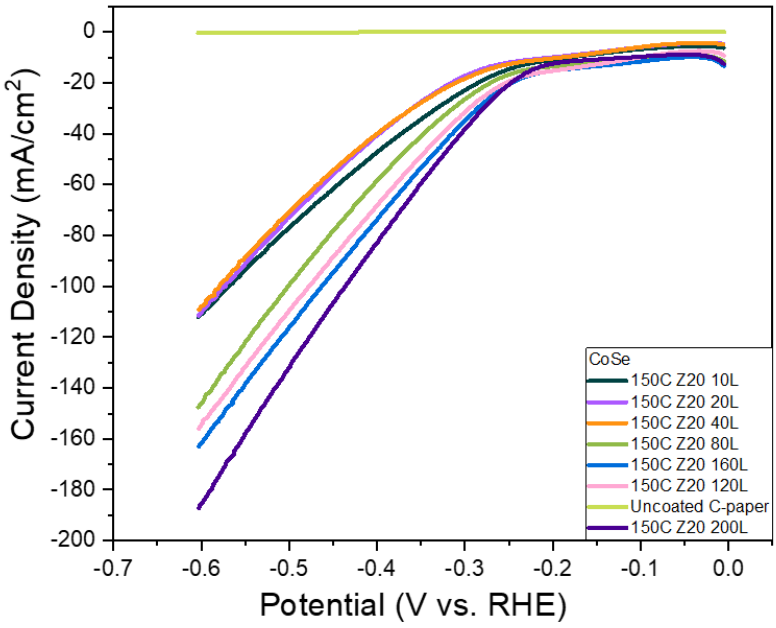


Figure 33. *LSV Results for Number of Layers Comparison (CoSe 150C Z20)*

The results show that performance generally increases with the number of layers, reaching its highest value with the 200-layer film. The fact that the 120-layer film takes a value between 80 and 160 layers confirms this monotonic trend and indicates that there is no random fluctuation. This regular increase reveals that performance improves with the number of layers up to 200. When the catalytic power of CoSe is compared with the results of uncoated carbon paper, it is seen that the 200L parameter leads to an approximately 420-fold catalytic improvement compared to the uncoated substrate.

The calculated Tafel slope values are as follows: 387 mV/dec for 10L, 401 mV/dec for 20L, 410 mV/dec for 40L, 397 mV/dec for 80L, 362 mV/dec for 120L, 358 mV/dec for 160L, and 339 mV/dec for 200L in Figure 34. Accordingly, the Tafel slope generally decreases as the number of layers increases, and the sample with the highest number of layers gave the lowest slope (200L, 339 mV/dec). This decrease indicates that the increasing active region density as the number of layers increases kinetically facilitates the reaction; more active regions accelerate the current increase per overvoltage, thus lowering the Tafel slope.

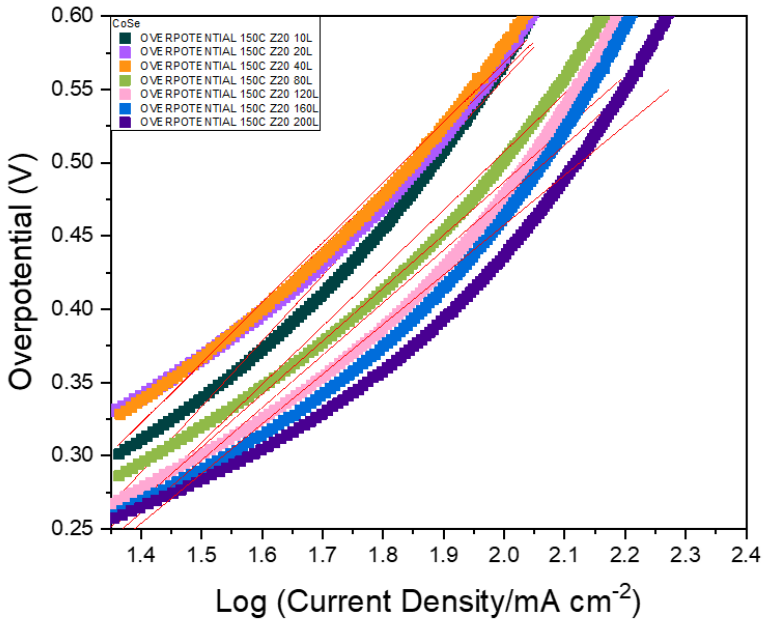


Figure 34. *Tafel Slope Analysis for Number of Layers Comparison (CoSe 150C Z20)*

At low voltage (−0.2 V), the load transfer resistances were measured as follows: ~100 Ω for 10L, ~100 Ω for 20L, ~90 Ω for 40L, ~60 Ω for 80L, ~60 Ω for 120L, ~50 Ω for 160L, and ~70 Ω for 200L (Figure 35). Thin films (10L, 20L) yielded the largest semicircles (~100 Ω), while films with a greater number of layers (80L–200L) showed lower Rct values (~50–70 Ω). The fact that uncoated carbon paper yielded the highest Rct (>100 Ω) confirms that CoSe provides catalytic activity even at low voltage.

At -0.4 V, the charge transfer resistances decreased for all layers: 200L gave the lowest Rct (~15 Ω), followed by 160L (~25 Ω), 120L (~30 Ω), and 80L (~35 Ω); films with fewer layers exhibited higher values (~40 Ω for 10L, ~50 Ω for 40L, ~55 Ω for 20L). At this potential, all CoSe layers still performed better than uncoated carbon paper.

At -0.5 V, the Rct values decreased for all layers: 200L gave the lowest Rct (~3 Ω), followed by 160L (~3.5 Ω) and 120L (~4 Ω); Films with fewer layers show higher values (~7 Ω for 80L, ~8 Ω for 10L, ~10 Ω for 20L, ~12 Ω for 40L). Films with 80 layers and above continue to give the smallest radius.

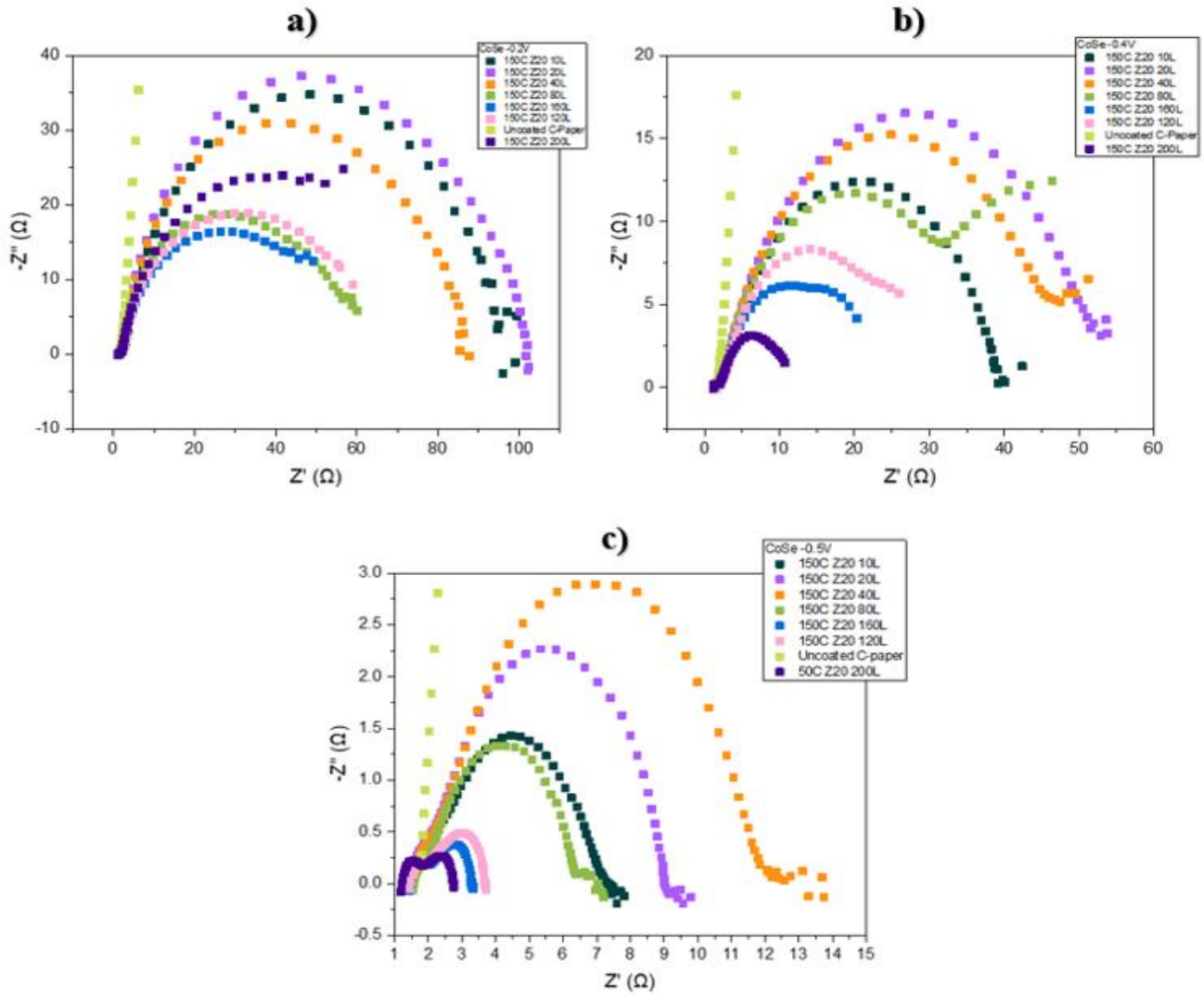


Figure 35. *EIS Results for Number of Layers Comparison (CoSe 150C Z20) at a) -0.2 V, b) -0.4 V and c) -0.5 V*

Table 6. *ECSA Results for Number of Layers Comparison (CoSe 150C Z20)*

PARAMETERS	ECSA (F/cm^2)
Z20 10L	1.41
Z20 20L	0.61
Z20 40L	0.93
Z20 80L	1.49
Z20 120L	3.52
Z20 160L	6.33
Z20 200L	25.5

To evaluate the effect of the number of layers on the active surface area, electrochemical active surface area (ECSA) calculations were performed for different numbers of layers at the Z20 distance. The obtained values are as follows: 1.41 F/cm^2 for 10L, 0.61 F/cm^2 for 20L, 0.93 F/cm^2 for 40L, 1.49 F/cm^2 for 80L, 3.52 F/cm^2 for 120L, 6.33 F/cm^2 for 160L, and 25.5 F/cm^2 for 200L. Accordingly, the highest active surface area was obtained with the highest number of layers (200L, 25.5 F/cm^2). ECSA values increase as the number of layers increases; the increase accelerates especially after 120 layers and reaches its highest value at 200 layers. Accordingly, the ECSA results are in complete consistency with the monotonic performance increase observed in CV and LSV, and the monotonic decrease in the Tafel slope.

3.3. Ruthenium-Decorated Cobalt Selenide (RuCoSe)

This section will examine the effects of spraying distance and then the number of layers on RuCoSe coatings, and the electrochemical techniques used for each parameter set (CV, LSV, EIS, Tafel, and ECSA) will be discussed in detail. Tested only at 150 °C and in an acidic electrolyte (0.5 M H_2SO_4, pH 0).

3.3.1. Influence of Distance

To evaluate the sensitivity of the RuCoSe catalyst to the spraying distance, films produced at 150 °C and 10 layers were characterized by cyclic voltammetry at four different distances (Z10, Z20, Z30, Z40) as shown in Figure 36. Cathodic current densities measured at a potential of −0.6 V (RHE) were obtained as follows: ~ −150 mA/cm^2 for Z10, ~ −130 mA/cm^2 for Z20, ~ −145 mA/cm^2 for Z30, and ~ −155 mA/cm^2 for Z40. While the highest performance was exhibited at the Z40 distance (~ −155 mA/cm^2), all distances yielded high and similar values between ~ −130 and −155 mA/cm^2. The performance difference between the distances is quite small; Even the difference between Z20, which gives the lowest value (~ −130 mA/cm^2), and Z40, which gives the highest value, is very small.

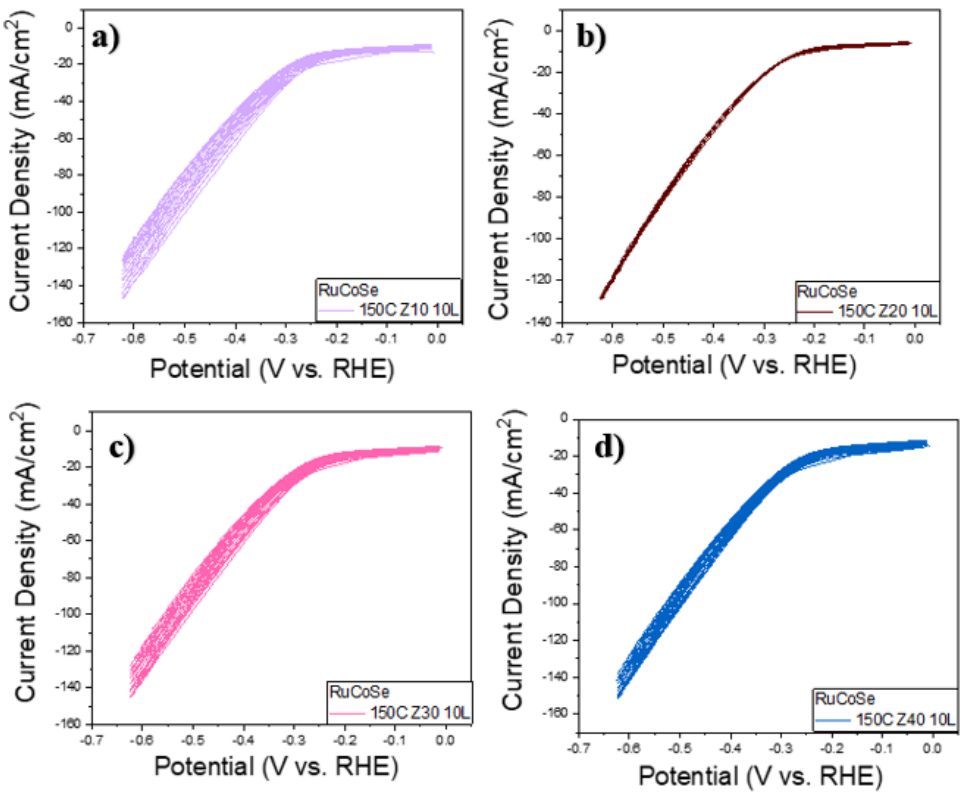


Figure 36. *CV of RuCoSe films coated (150 °C, 10 L) with different distances from a)10 mm, b)20 mm, c)30 mm and d)40 mm.*

Cathodic current densities measured at a potential of -0.6 V (RHE) were obtained as follows: ~ −130 mA/cm^2 for Z10, ~ −130 mA/cm^2 for Z20, ~ −135 mA/cm^2 for Z30, and ~ −138 mA/cm^2 for Z40 (Figure 37). Accordingly, the performance ranking is Z40 > Z30 > Z10 ≈ Z20, with all distances falling within a very narrow range between ~ −130 and −138 mA/cm^2.

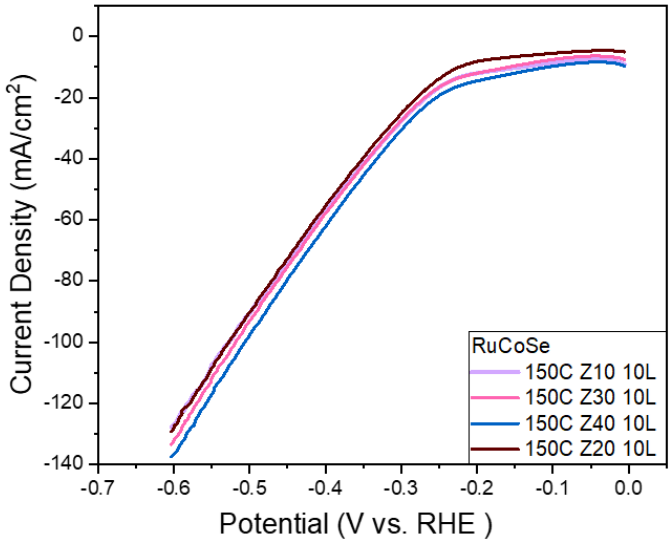


Figure 37. LSV Results for Distance Comparison (RuCoSe 150C 10L)

The LSV and CV results correlate with each other. All distances are very close and exhibit high performance; the difference between distances is only ~8 mA/cm^2. This demonstrates that RuCoSe offers consistent performance for all spray geometries. The lack of need for extremely precise control of the spray distance facilitates the repeatability and scalability of the production process.

The calculated Tafel slopes are as follows: 398 mV/dec for Z10, 387 mV/dec for Z20, 390 mV/dec for Z30, and 392 mV/dec for Z40 (Figure 38). While the lowest slope was obtained at distance Z20 (387 mV/dec), all distances were within an extremely narrow range of 387–398 mV/dec. This uniform distribution of Tafel slopes confirms the observation in other methods that the results are minimally affected by distance variation. The fact that the slope difference between distances is limited to only ~11 mV/dec indicates that the reaction kinetics are largely independent of the spray distance.

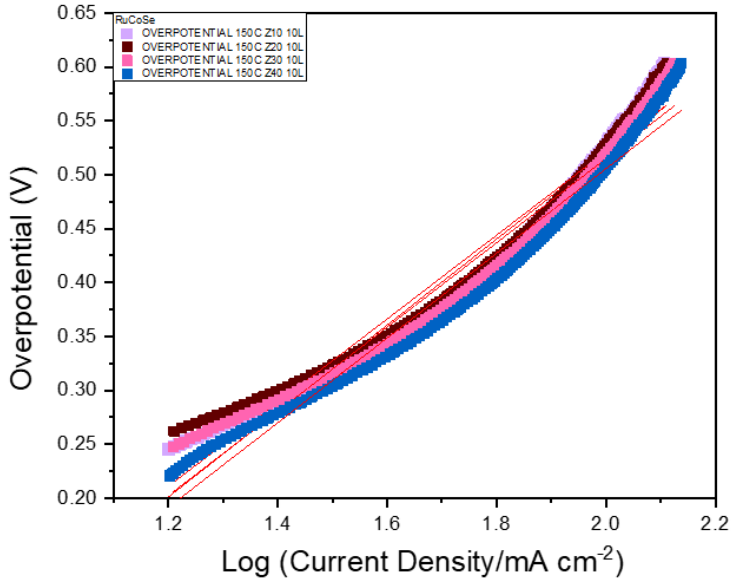


Figure 38. *Tafel Slope Analysis for Distance Comparison (RuCoSe 150C 10L)*

Electrochemical impedance spectroscopy measurements were performed at three different overvoltages (−0.2 V, −0.4 V, and −0.5 V). At the low voltage (−0.2 V), all distances were close together and exhibited low charge transfer resistances: Z40 gave the lowest Rct (~70 Ω), while Z20 was measured at ~75 Ω, and Z10 and Z30 at ~80 Ω (Figure 39a). The closeness of the semicircles at this potential is evidence of how little they are affected by the change in distance. At −0.4 V, the charge transfer resistances decreased for all distances, falling to the range of 18–30 Ω. At this potential, Z20 gives the lowest Rct (~18 Ω), followed by Z40 (~25 Ω), Z10 (~28 Ω), and Z30 (~30 Ω) in Figure 39b. The fact that the values remain within this narrow range indicates that the robustness to distance variation is maintained even at increasing voltage. At -0.5 V, the Rct values drop to extremely low levels (4.5–5.5 Ω) for all distances (Figure 39c). At this potential, Z20 and Z40 give the lowest Rct (~4.5 Ω), while Z30 (~5 Ω) and Z10 (~5.5 Ω) exhibit very close values; the ranking is Z20 ≈ Z40 > Z30 > Z10.

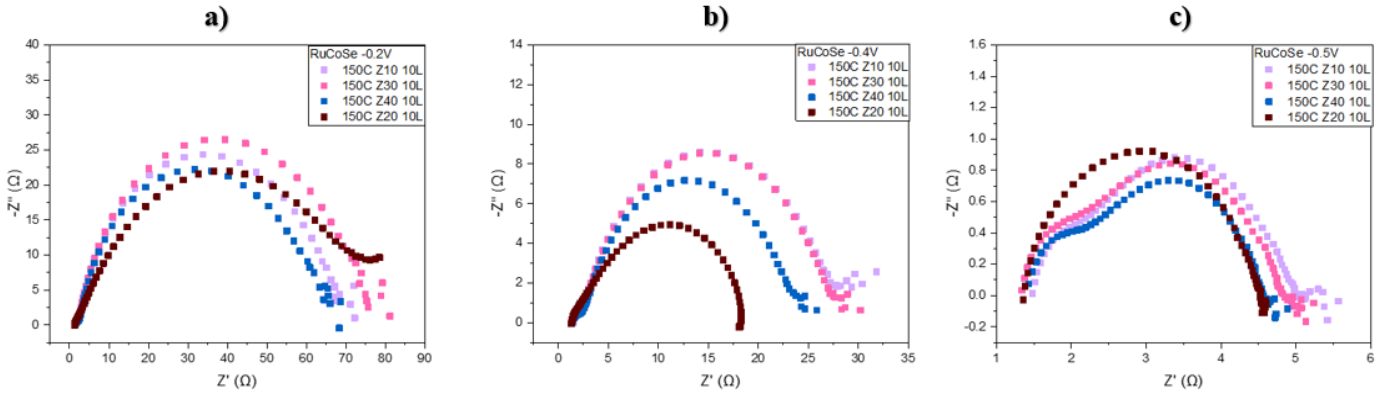


Figure 39. *EIS Results for Distance Comparison (RuCoSe 150C 10L) at a) -0.2 V, b) -0.4 V, and c) -0.5 V*

The results show that RuCoSe is resistant to distance variation and that different distances exhibit similar performance; in CV, Z40 provides slightly the highest current, while in Tafel and EIS analyses, Z20 provides the lowest slope and load transfer resistance. However, these differences are quite limited, and no distance parameter has a significant advantage over the others. Therefore, this allows us to select the appropriate parameter for comparison. To best compare two materials (RuCoSe and CoSe) with similar structures and using the same electrolyte and electrode types, the optimum distance selection was chosen as Z20, similar to that of CoSe.

Table 7. *ECSA Results for Distance Comparison (RuCoSe 150C 10L)*

PARAMETERS	ECSA (F/cm^2)
Z10 10L	0.69
Z20 10L	2.19
Z30 10L	0.96
Z40 10L	1.09

To evaluate the effect of spray distance on the active surface area, electrochemical active surface area (ECSA) measurements were performed at 50, 100, 150, 200, and 250 mV for films produced at 150 °C and 10 layers. ECSA values were calculated from the double-layer capacitance measured in a non-Faradaic potential window at different scan rates. The obtained values are as follows: 0.69 F/cm^2 for Z10, 2.19 F/cm^2 for Z20, 0.96 F/cm^2 for Z30, and 1.09 F/cm^2 for Z40. Accordingly, the highest active surface area was provided by the Z20 distance (2.19 F/cm^2), which is approximately two to three times higher than the other distances. The fact that the Z20 distance yielded the highest ECSA indicates that this distance covers a 1 cm^2 area most homogeneously, creating the most accessible surface area. These results explain why Z20, which provides the highest active surface area, was chosen as one of the optimum parameters.

3.3.2. Influence of Coating Layers

To ensure proper use, films with varying layer counts from 10L to 160L were produced while keeping the Z20 distance (considered optimum) constant, and characterized using CV, LSV Tafel slope, EIS, and electrochemically active surface area (ECSA) techniques. The effect of the number of layers on catalytic performance was evaluated using CV with films produced at different layer numbers (10L–160L) at the Z20 distance (Figure 40). Cathodic current densities measured at a potential of -0.6 V (RHE) were obtained as follows: ~ −130 mA/cm^2 for 10L, ~ −150 mA/cm^2 for 20L, ~ −200 mA/cm^2 for 40L, ~ −230 mA/cm^2 for 80L, ~ −165 mA/cm^2 for 120L, and ~ −195 mA/cm^2 for 160L. Accordingly, the highest performance was exhibited by the 80-layer film (~ −230 mA cm^2), which is the maximum value shown by RuCoSe.

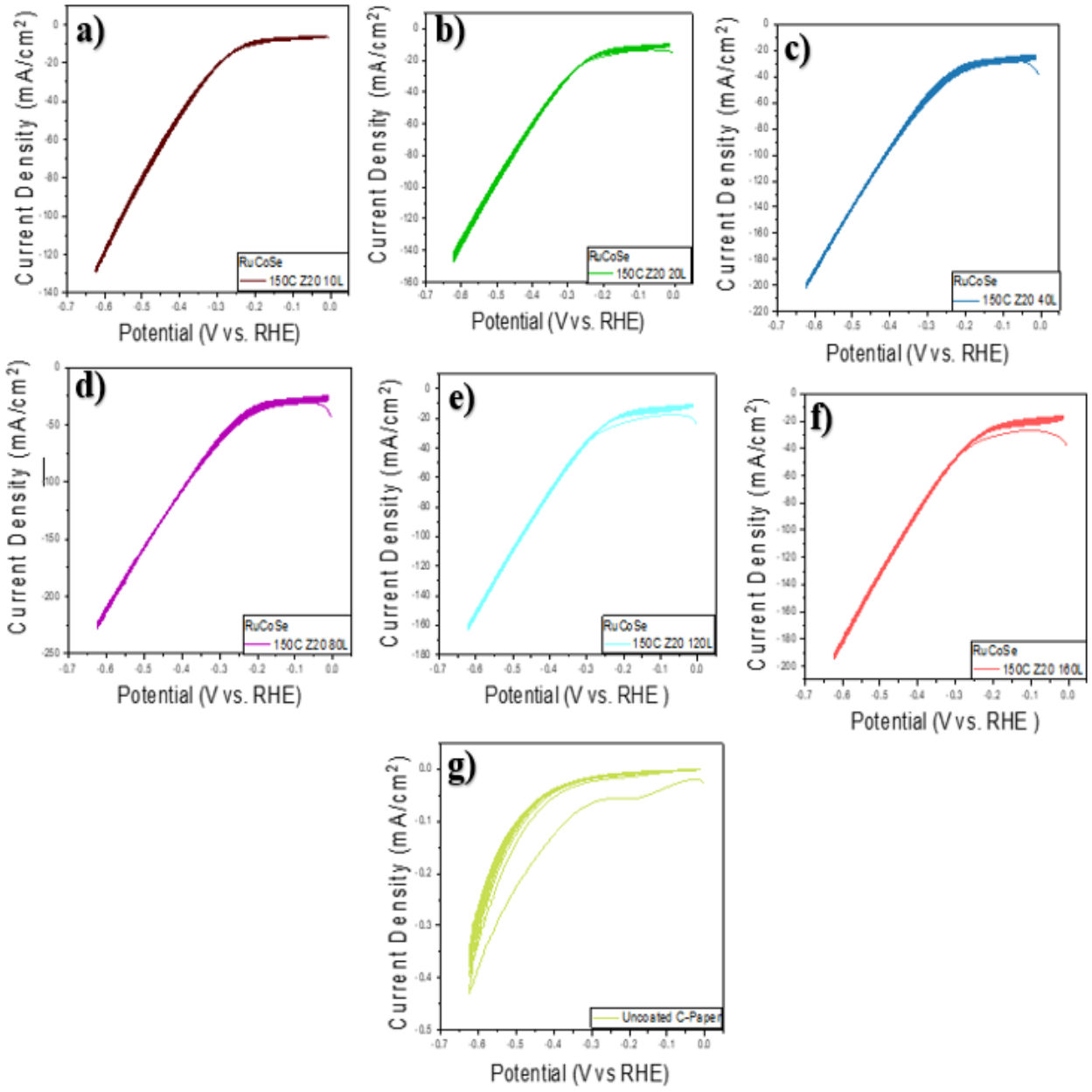


Figure 40. *CV Results of RuCoSe Films (150 °C, Z20) coated with a) 10 layers, b) 20 layers, c) 40 layers, d) 80 layers, e) 120 layers, f) 160 layers, g) 200 layers and h) Uncoated C-paper*

Performance increases as the number of layers increases, up to 80 layers, and reaches its peak value. A very significant jump (from ~ −130 to ~ −230 mA/cm^2) was observed, particularly when transitioning from 20 to 40 layers. After the peak, it begins to decrease; results of ~ −165 mA/cm^2 were obtained at 120 layers, and ~ −195 mA/cm^2 at 160 layers. The possible reason for this peak behavior is the balance between film thickness and active surface accessibility. Initially, as the number of layers increases, the total active material and therefore the current increase; however, after the film thickness exceeds a certain number of layers (above 80 layers), the active sites in the substrates may not have sufficient access to the electrolyte, or the increased thickness may limit

electrolyte and hydrogen bubble diffusion. Therefore, 80 layers have emerged as the optimal thickness, providing the best balance between the amount of active material and the accessible surface area. The catalytic power of RuCoSe is clearly different when compared to uncoated carbon paper. Uncoated carbon paper shows almost no catalytic activity in the acidic electrolyte (~ −0.45 mA/cm^2). This indicates that all measured hydrogen formation current originates directly from the catalyst coating, with very little contribution from the carbon paper substrate. Considering this fundamental value, the current of ~ −230 mA/cm^2 shown by the RuCoSe 80 layered sample contributes to an approximately 510 times catalytic improvement compared to the uncoated substrate. This striking difference clearly demonstrates that ruthenium-decorated cobalt selenide is an extremely effective hydrogen formation catalyst in an acidic environment and is the source of the observed high performance.

The cathodic current densities measured at a potential of -0.6 V (RHE) at the Z20 distance were obtained as follows: ~ −130 mA/cm^2 for 10L, ~ −145 mA/cm^2 for 20L, ~ −190 mA/cm^2 for 40L, ~ −223 mA/cm^2 for 80L, ~ −160 mA/cm^2 for 120L, and ~ −190 mA/cm^2 for 160L (Figure 41). Accordingly, the performance ranking is 80L > 40L ≈ 160L > 120L > 20L > 10L, with the highest current being provided by the 80-layer film (~ −223 mA/cm^2).

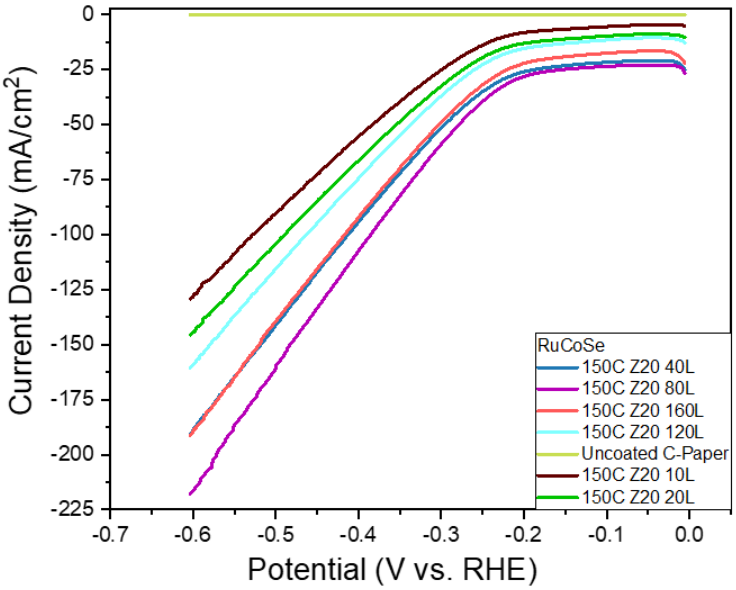


Figure 41. *LSV Results for Number of Layers Comparison (RuCoSe 150C Z20)*

The LSV results confirm the CV results. In both techniques, 80 layers stand out as the optimal thickness, and performance decreases beyond this point. Furthermore, the fact that 40 and 160 layers yield almost identical current densities (~ −190 mA/cm^2) indicates that these two different thicknesses exhibit similar catalytic behavior.

As observed in CV, a significant performance increase is also seen in LSV as the number of layers increases from low (10L, 20L) to medium (40L). This indicates that RuCoSe requires a certain minimum number of layers to reach its optimal catalytic activity, but performance becomes limited after this optimum number of layers is exceeded (above 80L). Furthermore, the difference between

the obtained values and those of uncoated carbon paper is very large. Considering the approximately negligible current (~ −0.45 mA/cm²) provided by uncoated carbon paper in an acidic environment, the ~ −223 mA/cm² current provided by the RuCoSe 80-layer sample shows approximately 495 times greater catalytic activity compared to the uncoated substrate.

The calculated values are 387 mV/dec for 10L, 482 mV/dec for 20L, 500 mV/dec for 40L, 483 mV/dec for 80L, 407 mV/dec for 120L, and 458 mV/dec for 160L (Figure 42). The variation is not monotonic and does not show a systematic increasing trend with the number of layers: the lowest apparent slope belongs to the thinnest film (10L, 387 mV/dec) and the highest slope to 40L (500 mV/dec), while 20L, 80L, and 160L are in the range of 458–483 mV/dec.

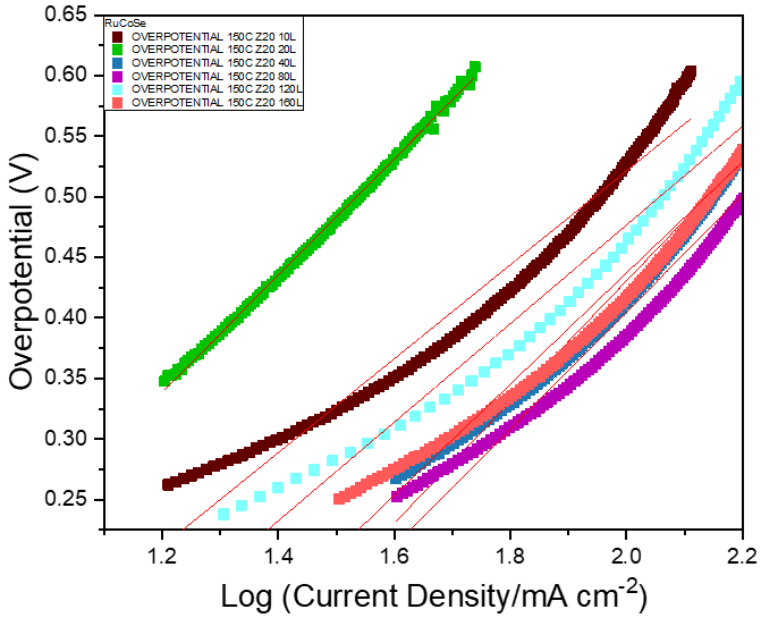


Figure 42. *Tafel Slope Analysis for Number of Layers Comparison (RuCoSe 150C Z20)*

The effect of the number of layers on the charge transfer behavior was evaluated at three different voltages (−0.2 V, −0.4 V, and −0.5 V), as shown in Figure 43.

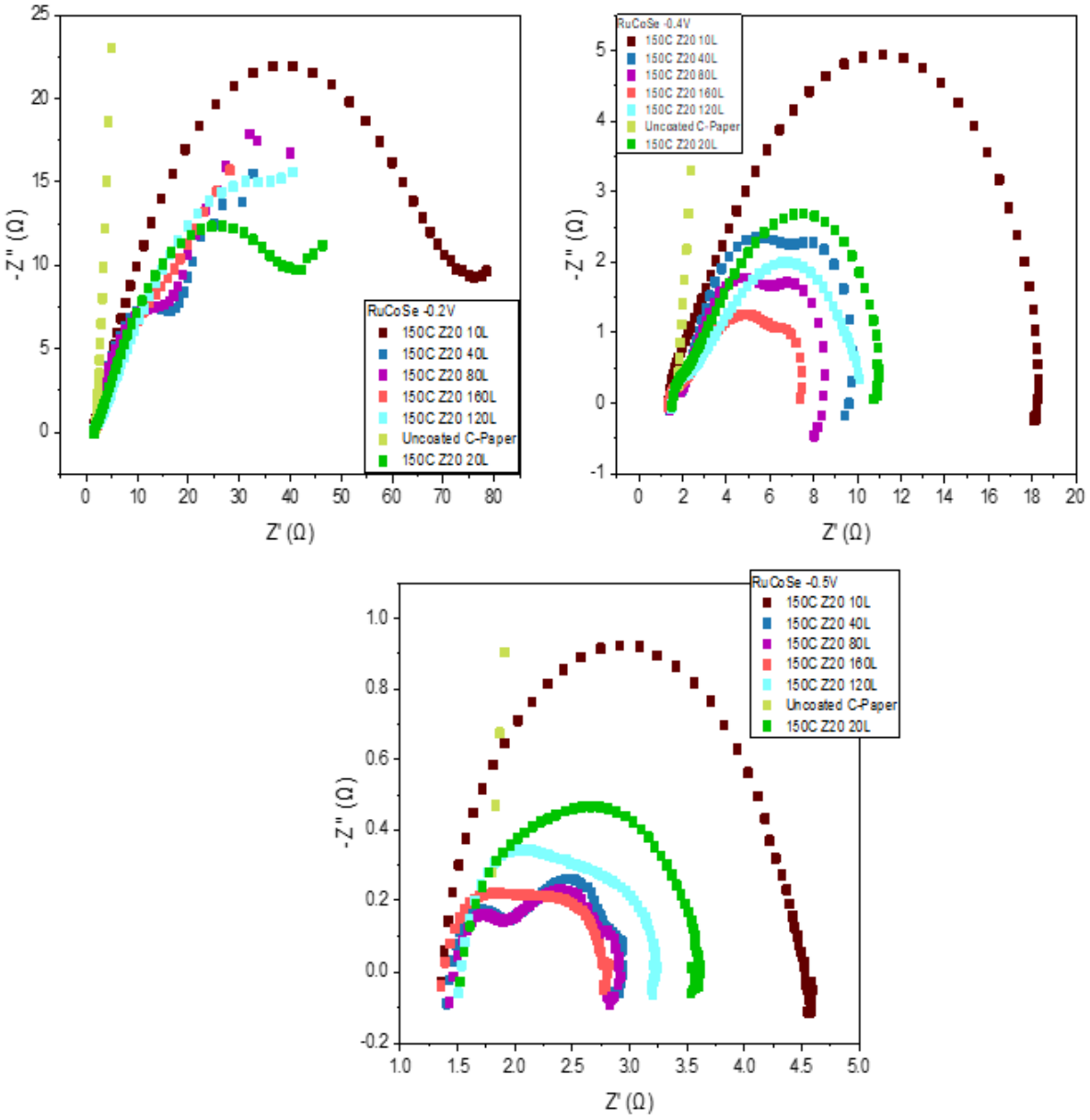


Figure 43. *EIS Results for Number of Layers Comparison (RuCoSe 150C Z20) at a) -0.2 V, b) -0.4 V and c) -0.5 V)*

At the low voltage (−0.2 V), only the 10-layer (~75 Ω) and 20-layer (~55 Ω) films showed complete (closed) semicircle curves. In contrast, thicker films (40L, 80L, 120L, 160L) and uncoated carbon paper showed incomplete semicircles (>80 Ω); in these samples, the charge transfer resistance remained too large to be resolved at −0.2 V. The fact that thin films showed complete semicircles at this potential indicates that the charge transfer process can be clearly defined even at low overvoltage. In measurements at -0.4 V, charge transfer resistances decreased significantly for all layer numbers, and the semicircular curves became fully visible. At this potential, the 10-layer film gave the highest Rct (~18 Ω), while the resistance decreased as the number of layers increased: ~11 Ω for 20L, ~9 Ω for 40L, ~8 Ω for 80L, ~10 Ω for 120L, and ~7 Ω for 160L. The lowest Rct value

was observed in the 160-layer film (~7 Ω). At -0.5 V, Rct values decreased further for all samples. At this potential, the 10-layer film gave the highest Rct (~4.5 Ω), while the 160-layer film gave the lowest Rct (~2.25 Ω). The number of layers exhibited the following values: ~3.5 Ω for 20L, ~2.8 Ω for 40L, ~2.8 Ω for 80L, and ~3.25 Ω for 120L. The fact that all samples yielded such low resistances demonstrates that RuCoSe exhibits good load transfer behavior under high overvoltage.

Table 8. *ECSA Results for Number of Layers Comparison (RuCoSe 150C Z20)*

PARAMETERS	ECSA(F/cm^2)
Z20 10L	2.19
Z20 20L	27.25
Z20 40L	3.73
Z20 80L	55.5
Z20 120L	83.75
Z20 160L	77.75

To evaluate the effect of the number of layers on the active surface area, electrochemical active surface area (ECSA) calculations were performed for different numbers of layers at the Z20 distance. The obtained values are as follows: 2.19 F/cm^2 for 10L, 27.25 F/cm^2 for 20L, 3.73 F/cm^2 for 40L, 55.5 F/cm^2 for 80L, 83.75 F/cm^2 for 120L, and 77.75 F/cm^2 for 160L. As a general trend, ECSA increases significantly with increasing number of layers; the highest active surface area is obtained in the 120-layer film (83.75 F/cm^2). The high ECSA values obtained are consistent with the high catalytic current densities exhibited by RuCoSe in other methods as well, confirming that the material has many accessible active sites.

3.4. RuCoSe and CoSe Comparison

The crystal structure of CoSe and RuCoSe were characterized by X-ray diffractometer (Malvern PANanalytical Empyrean Series-3 diffractometer, Cu Kα radiation, Malvern Panalytical Ltd, 40 kV and 40 mA.). Figure 44 shows the XRD patterns of CoSe and RuCoSe samples. Both patterns yield diffraction peaks at the same 2θ positions: peaks around 34°, 46°, and 51°, and 62° are the main peaks of hexagonal CoSe (ICSD number 53959). The overlap of the peak positions without a detectable shift indicates that the small amount of Ru did not alter the crystal structure of the cobalt selenide phase. In the peaks associated with RuCoSe, no new and distinguishable diffraction peaks attributable to metallic ruthenium or ruthenium oxide were observed. This does not mean that ruthenium is absent from the structure; it is probably due to the ruthenium being present in very small grain sizes, consequently with low crystallinity and in low amounts. The relatively wide peaks in both samples are consistent with the nanocrystalline character of the material and the low bulk loading of the thin films obtained by spray coating. Small crystalline domains imply more grain boundaries and more low-coordination surface regions per unit mass, which can act as preferential active sites for HER. Consequently, the XRD findings provide a complementary framework to the electrochemical results, since the bulk phase remained largely unchanged. This suggests that the source of the performance difference should be sought at the surface and interface levels.

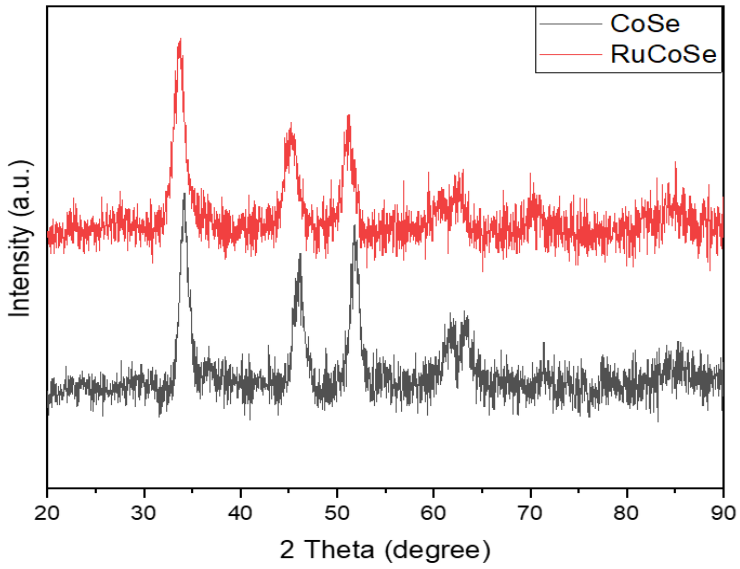


Figure 44. XRD of CoSe & RuCoSe

Since CoSe and RuCoSe catalysts were tested in 0.5 M H_2SO_4 (pH = 0) at 150 °C, and at the spraying distance of Z20, a direct comparison between these two materials can be made under identical conditions and with the same parameters. The only difference between the two samples is ruthenium in RuCoSe; therefore, all observed performance differences are directly because of ruthenium. In this section, the comparison was specifically made at 150 °C, at a spraying distance of 20 mm, and on 80-layer films. The reason for choosing this specific number of layers is that 80 layers has been determined as the optimal thickness for RuCoSe; RuCoSe performance peaks at 80 layers and decreases after this point. In contrast, in CoSe, performance continues to increase with the number of layers, and an optimal thickness has not yet been determined. Therefore, 80 layers constitutes a common reference point for comparing both catalysts.

Table 9. *150C Z20 80L RuCoSe & CoSe HER Results*

Method	CoSe	RuCoSe	Unit
CV	~ -165	~ -230	mA/cm^2
LSV	~ -150	~ -223	mA/cm^2
TAFEL SLOPE	397	483	mV/dec
EIS	7	2.8	Ω
ECSA	1.49	55.5	F/cm^2

In conclusion, this comparison reveals that ruthenium significantly improves the performance of the cobalt selenide catalyst both quantitatively and qualitatively. The presence of ruthenium has a positive effect on catalytic performance, manifesting as both an expansion of the active site where the reaction takes place and an improvement in charge transfer kinetics. Thus, it offers a much larger active site and enables the material to achieve high performance at lower layer numbers. In

this context, RuCoSe stands out as a catalyst that provides both higher performance and optimum results with less material due to its lower layer number compared to CoSe.

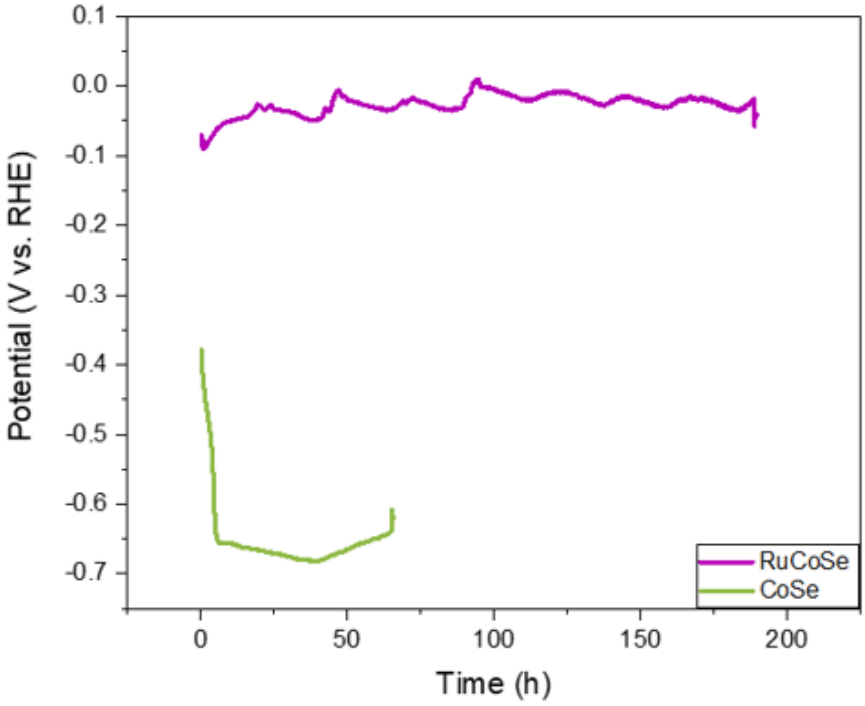


Figure 45. CP Results of RuCoSe & CoSe

Long-term stability tests were conducted for both materials at 150 °C Z20 80-layer conditions (150 °C Z20 80L) to directly determine whether the active sites were maintained under operating conditions (Figure 44). Measurements were performed in 0.5 M H_2SO_4 electrolyte, at a constant cathodic current density of 5 mA cm^{-2} and a recording interval of 300 seconds; the temperature was kept constant and the electrolyte was never refilled or changed.

Even at the beginning of the test, the two samples decompose: for the same current density, CoSe requires approximately −0.38 V, while for RuCoSe this value is −0.09 V. The decomposition over time proceeded in the opposite direction. RuCoSe exhibits an activation phase in which the potential shifts to -0.03 V within the first 15-20 hours; this recovery may be related to the completion of electrode wetting. In CoSe, however, the same range corresponds to a rapid decay in which the potential shifts to -0.65 V within the first five hours. This sharp, unidirectional shift indicates a rapid decrease in the number of accessible active sites. The potential of CoSe reached its most negative value at 35-40 hours, then showed a gradual increase, and based on this trend, the measurement was terminated at approximately 65 hours. The post-activation behavior of RuCoSe is characterized by a curve that repeats at regular intervals. Considering that the temperature was kept constant and the electrolyte was not changed, this pattern appears not to be caused by external interference; the ups and downs in the curve returning to the same level in each cycle suggest that the process is reversible. The absence of a similar periodicity in the CP curve of CoSe indicates that the gas retention and release behavior of the two electrodes is also different.

Consequently, RuCoSe showed no net increase in overvoltage during approximately 190 hours of continuous operation; the potential in the final phase remained less negative than the initial value. The emergence of such a trend despite the electrolyte not being replenished is a strong indication of the electrolyte's stability. The fact that RuCoSe maintained its stability for approximately three times the operating time of CoSe and at the lowest layer configuration demonstrates that the contribution of ruthenium decoration was not limited to the initial activity.

4. CONCLUSION & PERSPECTIVE

In this study, thin-film catalysts were fabricated on carbon paper by ultrasonic spray coating using colloidal inks containing three different nanomaterials: CZTS, CoSe, and RuCoSe. The effects of platform temperature, nozzle–substrate distance, number of deposited layers, and their interactions on hydrogen evolution reaction performance were systematically investigated. The results demonstrate that catalytic performance depends not only on the intrinsic properties of the catalyst but also strongly on the conditions used to form the coating. These parameters influence the overall electrochemical response by affecting solvent evaporation, material distribution, film continuity, catalyst loading, and charge transport pathways. Since film morphology is not directly characterized, the proposed relationships between coating conditions, film structure, and catalytic performance should be considered as interpretations supported by electrochemical results.

For CZTS, optimum coating conditions within the investigated parameter range were determined as a platform temperature of 150 °C, a spraying distance of Z20, and 10 layers. Among the variables investigated, platform temperature produced the most significant change in CZTS activity. The superior performance obtained at 150 °C was attributed to the favorable balance between isopropanol evaporation and nanoparticle organization during deposition. At lower temperatures, slower solvent removal could hinder the formation of effective interparticle contacts, while at 200 °C, excessively rapid evaporation could reduce film homogeneity and impair electrical conduction. Spraying distance and number of layers also affected the response, but their optimum values depend on temperature and on each other. This interaction confirms that coating parameters cannot be optimized independently.

CZTS exhibited significantly higher HER activity in the neutral electrolyte compared to the acidic electrolyte. This behavior suggests that the catalytic response is governed by a combination of electrolyte-dependent surface chemistry, interfacial stability, adsorption, and charge transfer processes, rather than solely by proton concentration. Discrete light measurements also revealed a reproducible photoreactive response, confirming the light-sensitive semiconductor character of CZTS. However, the limited difference between illuminated and dark LSV curves, particularly in the neutral electrolyte, indicates that further research is needed to achieve significant steady-state photoelectrocatalytic improvement. Nevertheless, these results demonstrate the potential of CZTS as a photoreactive HER catalyst and provide a basis for its further development for solar-assisted hydrogen production.

Cobalt selenide-based catalysts, CoSe and RuCoSe, exhibited high catalytic activity in acidic electrolytes. Under comparable measurement conditions, ruthenium addition improved both the current response and the electrochemically active surface area of CoSe. However, the two materials showed different layer-dependent behaviors. CoSe activity continued to increase with the number of layers deposited in the investigated range, suggesting that the optimum number of layers may not yet have been reached. In contrast, RuCoSe exhibited maximum performance at a specific number of layers, and further deposition after that did not provide any additional improvement. This difference demonstrates that the balance between catalyst loading, active surface accessibility, film resistance, and mass transfer is largely dependent on material composition. Consequently, catalyst identity and thin-film fabrication conditions should be considered together when designing high-performance electrodes.

From a methodological perspective, the study demonstrates the value of combining complementary electrochemical techniques, including CV, LSV, EIS, Tafel analysis, and ECSA measurements, where appropriate. These techniques describe different and non-equivalent aspects of electrode performance. LSV and CV characterize the overall current response, EIS provides comparative information about interfacial and through-film impedance, Tafel analysis describes the potential dependence of the current within the selected fitting region, and ECSA provides an estimate of electrochemically accessible surface area. The samples highlighted by the individual techniques were not always identical. Rather than representing contradictory results, these differences show that total catalytic performance is determined by several interconnected factors. A combined interpretation therefore provides a more reliable assessment than any single electrochemical descriptor.

Several directions for future research arise from these findings. Direct characterization by scanning electron microscopy and atomic force microscopy should be performed to verify the proposed relationships among coating parameters, film coverage, roughness, porosity, and cracking. Surface-sensitive composition techniques such as XPS or EDS will also help determine whether changes in elemental distribution or surface composition contribute to the observed electrochemical trends. When sufficient sample mass is available, BET analysis can provide additional surface area information for catalyst powders or coating materials. For CoSe, higher layer counts should be investigated to determine whether the activity ultimately reaches an optimum and to allow for a more comprehensive comparison with RuCoSe.

Long-term stability measurements for optimum CZTS, CoSe, and RuCoSe electrodes should also be expanded. Tests at higher current densities, along with post-stabilization structural and compositional characterization, will provide a more realistic assessment of their suitability for practical hydrogen production. Finally, the photoelectrochemical behavior of CZTS should be investigated through controlled light intensity and wavelength-dependent measurements, band gap and band alignment studies, and the creation of suitable heterostructures. These studies would clarify the origin of the photoresponse and could guide the development of more efficient CZTS-based photoelectrocatalysts. Overall, the present work demonstrates that ultrasonic spray coating provides a versatile route for producing nanomaterial-based HER electrodes and that careful control of composition and film-formation parameters is essential for developing low-cost, efficient, and stable hydrogen-evolution catalysts.

REFERENCES

Ahmaruzzaman, M. *et al.* (2025) 'Hydrogen Generation by Photolysis of Water Vis-à-Vis Other Conventional and Advanced Non-conventional Methods of Hydrogen Production—A Review', *Journal of Inorganic and Organometallic Polymers and Materials*, 35(1), pp. 22–45. Available at: https://doi.org/10.1007/s10904-024-03272-4.

Anita, N. *et al.* (2023) 'Linear polarization resistance (LPR) technique for corrosion measurements', *Electrochemical and Analytical Techniques for Sustainable Corrosion Monitoring*. Elsevier, pp. 59–80. Available at: https://doi.org/10.1016/B978-0-443-15783-7.00005-0.

Armbruster, B.L. *et al.* (2025) 'The Effects of Plasma Cleaning on Carbon and Hydrocarbon-contaminated Samples and Quantification of Decontamination in the Scanning Electron Microscope', *Microscopy and Microanalysis*, 31(Supplement_1). Available at: https://doi.org/10.1093/mam/ozaf048.238.

Benramache, S., Benhaoua, B. and Bentrah, H. (2013) 'Preparation of transparent, conductive ZnO:Co and ZnO:In thin films by ultrasonic spray method', *Journal of Nanostructure in Chemistry*, 3(1), p. 54. Available at: https://doi.org/10.1186/2193-8865-3-54.

Bose, S. *et al.* (2013) 'Process Optimization of Ultrasonic Spray Coating of Polymer Films', *Langmuir*, 29(23), pp. 6911–6919. Available at: https://doi.org/10.1021/la4010246.

Digraskar, R. V. *et al.* (2017) 'Enhanced Hydrogen Evolution Reactions on Nanostructured Cu2ZnSnS4 (CZTS) Electrocatalyst', *Applied Surface Science*, 412, pp. 475–481. Available at: https://doi.org/10.1016/j.apsusc.2017.03.262.

Digraskar, R.V. *et al.* (2018) 'Enhanced electrocatalytic hydrogen generation from water via cobalt-doped Cu2ZnSnS4 nanoparticles', *RSC Advances*, 8(36), pp. 20341–20346. Available at: https://doi.org/10.1039/C8RA01886C.

Digraskar, R.V. *et al.* (2019) 'CZTS Decorated on Graphene Oxide as an Efficient Electrocatalyst for High-Performance Hydrogen Evolution Reaction', *ACS Omega*, 4(4), pp. 7650–7657. Available at: https://doi.org/10.1021/acsomega.8b03587.

Dixit, M.B. *et al.* (2018) 'Catalyst Layer Ink Interactions That Affect Coatability', *Journal of The Electrochemical Society*, 165(5), pp. F264–F271. Available at: https://doi.org/10.1149/2.0191805jes.

Elgrishi, N. *et al.* (2018) 'A Practical Beginner's Guide to Cyclic Voltammetry', *Journal of Chemical Education*, 95(2), pp. 197–206. Available at: https://doi.org/10.1021/acs.jchemed.7b00361.

van der Heijden, O. *et al.* (2024) 'Tafel Slope Plot as a Tool to Analyze Electrocatalytic Reactions', *ACS Energy Letters*, 9(4), pp. 1871–1879. Available at: https://doi.org/10.1021/acsenergylett.4c00266.

Hu, X. *et al.* (2024) 'Morphology and Stoichiometry Dependent Electrocatalytic Activity of Cu2ZnSnS4 for Hydrogen Evolution Reaction (HER) with Addition of Nonionic Surfactants', *Electrocatalysis*, 15(1), pp. 1–9. Available at: https://doi.org/10.1007/s12678-023-00846-7.

Johnson Andi (2025) ‘Electrochemical surface area (ECSA) evaluation in electrocatalysis: principles, measurement techniques, and future perspectives’, *Journal of Engineering in Industrial Research*, 6(3), pp. 212–222.

Kahyarian, A., Singer, M. and Nesic, S. (2016) ‘Modeling of uniform CO2 corrosion of mild steel in gas transportation systems: A review’, *Journal of Natural Gas Science and Engineering*, 29, pp. 530–549. Available at: https://doi.org/10.1016/j.jngse.2015.12.052.

Kong, D. *et al.* (2014) ‘CoSe2 nanoparticles grown on carbon fiber paper: an efficient and stable electrocatalyst for hydrogen evolution reaction’, *Journal of the American Chemical Society*, 136(13), pp. 4897–4900. Available at: https://doi.org/10.1021/ja501497n.

Kumar, R., Kumar, A. and Pal, A. (2021) ‘An overview of conventional and non-conventional hydrogen production methods’, *Materials Today: Proceedings*, 46, pp. 5353–5359. Available at: https://doi.org/10.1016/j.matpr.2020.08.793.

Kush, P. *et al.* (2015) ‘Efficient hydrogen/oxygen evolution and photocatalytic dye degradation and reduction of aqueous Cr(vi) by surfactant free hydrophilic Cu2ZnSnS4 nanoparticles’, *Journal of Materials Chemistry A*, 3(15), pp. 8098–8106. Available at: https://doi.org/10.1039/C4TA06551D.

Lasia, A. (2019) ‘Mechanism and kinetics of the hydrogen evolution reaction’, *International Journal of Hydrogen Energy*, 44(36), pp. 19484–19518. Available at: https://doi.org/10.1016/j.ijhydene.2019.05.183.

Lazanas, A.Ch. and Prodromidis, M.I. (2023) ‘Electrochemical Impedance Spectroscopy─A Tutorial’, *ACS Measurement Science Au*, 3(3), pp. 162–193. Available at: https://doi.org/10.1021/acsmeasuresciau.2c00070.

Liu, L. *et al.* (2024) ‘Ru incorporated into Se vacancy-containing CoSe2 as an efficient electrocatalyst for alkaline hydrogen evolution’, *Nanoscale*, 16(39), pp. 18421–18429. Available at: https://doi.org/10.1039/D4NR02735C.

Liu, T. *et al.* (2015) ‘An amorphous CoSe film behaves as an active and stable full water-splitting electrocatalyst under strongly alkaline conditions’, *Chemical Communications*, 51(93), pp. 16683–16686. Available at: https://doi.org/10.1039/C5CC06892D.

Marcelo M. Tusi a, M.B. a, R.W.R.V.-S. a, O.V.C. a, J.C.V. b, F.J.A. b, A.O.N. a, M.L. a, E.V.S. a (2010) ‘Preparation of PtRu/C electrocatalysts by hydrothermal carbonization using different carbon sources’, in M.D.S.H.P.J.J.M. and P.R. E.M. Gaigneaux (ed.) *Studies in Surface Science and Catalysis*, pp. 551–554. Available at: https://doi.org/10.1016/S0167-2991(10)75106-5.

McCay, M.H. and Shafiee, S. (2020) ‘Hydrogen’, *Future Energy*. Elsevier, pp. 475–493. Available at: https://doi.org/10.1016/B978-0-08-102886-5.00022-0.

Ortiz-Ortega, E. *et al.* (2021) ‘Aging of plasma-activated carbon surfaces: Challenges and opportunities’, *Applied Surface Science*, 565, p. 150362. Available at: https://doi.org/10.1016/j.apsusc.2021.150362.

Pozzati, M. *et al.* (2024) ‘Systematic Investigation on the Surfactant-Assisted Liquid-Phase Exfoliation of MoS2 and WS2 in Water for Sustainable 2D Material Inks’, *physica status solidi (RRL) – Rapid Research Letters*, 18(9). Available at: https://doi.org/10.1002/pssr.202400039.

Qadeer, M.A. *et al.* (2024) 'A review on fundamentals for designing hydrogen evolution electrocatalyst', *Journal of Power Sources*, 613, p. 234856. Available at: https://doi.org/10.1016/j.jpowsour.2024.234856.

Qu, Y. *et al.* (2014) 'Influence of reaction conditions on the properties of solution-processed Cu2ZnSnS4 nanocrystals', *Materials Research Express*, 1(4), p. 045040. Available at: https://doi.org/10.1088/2053-1591/1/4/045040.

Ramírez, Á. *et al.* (2025) 'Sustainable electrochemical production of H_2O_2 on carbon blacks: Structural properties as key drivers', *Electrochimica Acta*, 532, p. 146508. Available at: https://doi.org/10.1016/j.electacta.2025.146508.

Raveendran, A., Chandran, M. and Dhanusuraman, R. (2023) 'A comprehensive review on the electrochemical parameters and recent material development of electrochemical water splitting electrocatalysts', *RSC Advances*, 13(6), pp. 3843–3876. Available at: https://doi.org/10.1039/D2RA07642J.

Shinagawa, T., Garcia-Esparza, A.T. and Takanabe, K. (2015) 'Insight on Tafel slopes from a microkinetic analysis of aqueous electrocatalysis for energy conversion', *Scientific Reports*, 5(1), p. 13801. Available at: https://doi.org/10.1038/srep13801.

Shukla, S. *et al.* (2017) 'Experimental and Theoretical Analysis of Ink Dispersion Stability for Polymer Electrolyte Fuel Cell Applications', *Journal of The Electrochemical Society*, 164(6), pp. F600–F609. Available at: https://doi.org/10.1149/2.0961706jes.

Sliz, R., Czajkowski, J. and Fabritius, T. (2020) 'Taming the Coffee Ring Effect: Enhanced Thermal Control as a Method for Thin-Film Nanopatterning', *Langmuir*, 36(32), pp. 9562–9570. Available at: https://doi.org/10.1021/acs.langmuir.0c01560.

Taherpour, A.A. and Mousavi, F. (2018) 'Carbon nanomaterials for electroanalysis in pharmaceutical applications', *Fullerens, Graphenes and Nanotubes*. Elsevier, pp. 169–225. Available at: https://doi.org/10.1016/B978-0-12-813691-1.00006-3.

Wan, C. *et al.* (2024) 'Unraveling and Resolving the Inconsistencies in Tafel Analysis for Hydrogen Evolution Reactions', *ACS Central Science*, 10(3), pp. 658–665. Available at: https://doi.org/10.1021/acscentsci.3c01439.

Wang, M. *et al.* (2018) 'Ni–Co–S–Se Alloy Nanocrystals: Influence of the Composition on Their in Situ Transformation and Electrocatalytic Activity for the Oxygen Evolution Reaction', *ACS Applied Nano Materials*, 1(10), pp. 5753–5762. Available at: https://doi.org/10.1021/acsanm.8b01418.

Wang, M. *et al.* (2019) 'Ruthenium-Decorated Cobalt Selenide Nanocrystals for Hydrogen Evolution', *ACS Applied Nano Materials*, 2(9), pp. 5695–5703. Available at: https://doi.org/10.1021/acsanm.9b01205.

Wang, M. *et al.* (2023) 'New Insights into the Surfactant-Assisted Liquid-Phase Exfoliation of Bi2S3 for Electrocatalytic Applications', *Catalysts*, 13(3), p. 551. Available at: https://doi.org/10.3390/catal13030551.

Wang, M. *et al.* (2024) ‘Tuning Surface Chemistry in 2D Layered BiOI by Facile Liquid-Phase Exfoliation for Enhanced Photoelectrocatalytic Oxygen Evolution’, *Small Structures*, 5(11). Available at: https://doi.org/10.1002/sstr.202400275.

Zhang, B. *et al.* (2020) ‘Colloidal Bi-doped Cs2Ag1–xNaxInCl6 nanocrystals: undercoordinated surface Cl ions limit their light emission efficiency’, *ACS Materials Letters*, 2(11), pp. 1442–1449. Available at: https://doi.org/10.1021/acsmaterialslett.0c00359.